COLA III. Radio Detection of AGN in Compact Moderate Luminosity Infra-Red Galaxies

R. Parra[1] , J. E. Conway, S. Aalto
Onsala Space Observatory, SE-439 92 Onsala, Sweden

P. N. Appleton
NASA Herschel Science Center, Mail Code 100-22, California Institute of Technology. 770 S. Wilson Blvd. Pasadena CA 91125

R. P. Norris
CSIRO Australia Telescope National Facility, P.O. Box 76, Epping, NSW 17 10, Australia

Y. M. Pihlström[2]
Department of Physics and Astronomy, UNM, 800 Yale Blvd NE, Albuquerque, NM 87131
and

L. J. Kewley
University of Hawaii, 2680 Woodlawn Drive, Honolulu, HI 96822

ABSTRACT

We present results from 4.8 GHz VLA and Global-VLBI observations of the northern half of the moderate FIR luminosity (median $L_{\rm IR} = 10^{11.01} L_{\odot}$) COLA sample of star-forming galaxies. VLBI sources are detected in a high fraction (20/90) of the galaxies observed. The radio luminosities of these cores ($\sim 10^{21}$ W Hz^{-1}) are too large to be explained by radio supernovae or supernova remnants and we argue that they are instead powered by AGN. These sub-parsec scale radio cores are preferentially detected toward galaxies whose VLA maps show bright 100-500 parsec scale nuclear radio components. Since these latter structures tightly follow the FIR to radio-continuum correlation for star-formation we conclude that the AGN powered VLBI sources are associated with compact nuclear starburst environments. The implications for possible starburst-AGN connections are discussed. The detected VLBI sources have a relatively narrow range of radio luminosity consistent with models in which intense compact Eddington-limited starbursts regulate the gas supply onto a central super-massive black hole. The high incidence of AGN radio cores in compact starbursts suggests little or no delay between the starburst phase and the onset of AGN activity.

Subject headings: galaxies: active — galaxies: starburst — infrared: galaxies — radio continuum: galaxies

[1]Now at European Southern Observatory, Alonso de Cordova 3107, Casilla 19001, Santiago 19, Chile

[2]Also Adjunct Astronomer at the National Radio Astronomy Observatory

1. Introduction

It seems likely that super-massive black holes (SMBH) are ubiquitous in galactic nuclei. The nuclear stellar-velocity dispersion and bulge-size to black hole mass correlations (Magorrian et al. 1998; Merloni et al. 2003; Häring & Rix 2004) indicate that most galaxies with central bulges should contain SMBHs at their centers. The presence of a SMBH is a necessary condition for AGN activity but only a small fraction of galaxies at any given time are strong AGN sources, implying that a decisive factor determining AGN luminosity is the gas feeding mechanism. While for Seyfert or LINER class AGN only relatively small black hole accretion rates are required (0.01 to $0.1\,M_{\odot}\,\mathrm{year}^{-1}$) gas originating in the galactic disk must lose angular momentum in order to be accreted onto the central black hole. Various mechanisms to achieve such momentum transfer and mass transport have been suggested (see review by Knapen 2004).

There is increasing observational evidence for an AGN-starburst connection (Davies et al. 2007; Heckman 2008; Prieto et al. 2005, 2007; Fathi et al. 2006). Plausibly such circumnuclear starbursts may play a role in removing angular momentum and so feeding the central black hole (Schartmann et al. 2010). Alternatively both nuclear starbursts and AGN could be independent consequences of a common gas transport mechanism into the centers of galaxies with no direct causal connection between the two phenomena. Understanding in detail the phenomenology of starburst and AGN activity, in particular whether one phase begins before the other, is important to test the nature of the starburst-AGN interrelationship.

Most detailed observational work so far on the starburst-AGN connection has studied starburst activity in samples of AGN (Davies et al. 2007). Here we adopt the alternative approach of searching for AGN activity in a far infrared-selected sample of star-forming galaxies known as COLA (Compact Objects in Low-power AGN, Corbett et al. 2002, 2003, see §2 for sample definition). Our principal means of identifying AGN activity in this sample is by searching for high brightness temperature VLBI radio cores. Classic optical emission line diagnostics (Baldwin et al. 1981; Veilleux & Osterbrock 1987; Kewley et al. 2001; Kauffmann et al. 2003) can be unreliable for such searches as an AGN may be obscured by dust in star-forming galaxies. High brightness-temperature radio emission is unambiguous evidence of an AGN, however a non-detection does not exclude an AGN because of the existence of both radio loud and radio quiet objects (see Zamfir et al. 2008, for a recent review); it follows that VLBI searches can only give a lower limit to the AGN fraction. It should be noted that while radio supernovae (SNe) can also generate compact radio emission they have a maximum luminosity which distinguishes them from AGN (see Corbett et al. 2002, and §5.1.4).

We have already published radio observations (Corbett et al. 2002) and optical spectroscopy results Corbett et al. (2003) for the $\delta < 0^{\circ}$ (COLA-S) part of the sample. Here we present radio and optical observations of the Northern half ($\delta > 0^{\circ}$) of the sample (COLA-N). This paper is organized as follows. In §2 we give an overview of the COLA project and previous observations. In §3 we describe our VLA, VLBI, optical spectroscopy and other observations and give an overview of the data reduction process. Our observational results are presented in §4 and our discussion in §5. Finally in §6 we list our major conclusions.

2. The COLA Project and Previous Observations

The COLA (Compact Objects in Low-power AGN) project has the primary goal of determining the relationship between AGN and other galactic properties (such as galactic structure, degree of interaction and star formation activity) in a moderate luminosity FIR selected sample. The sample contains all the galaxies in the *IRAS* Point Source Catalog (Beichman et al. 1988) with (a) flux densities at $60\,\mu$m greater than 4 Jy, (b) heliocentric velocities between 3500 and 7000 km s^{-1} (to minimize Malmquist bias) and (c) galactic latitude $|b|>10^{\circ}$ (to avoid confusion with galactic objects). The resulting sample has 217 galaxies of which 110 are located in the northern hemisphere (COLA-N) and 107 in the Southern hemisphere (COLA-S).

The COLA sample is selected at the same IR wavelength as the Revised Bright Galaxy Sample (RBGS see Sanders et al. (2003)) but with a

flux limit which is somewhat smaller (4 Jy versus 5.24 Jy) plus an additional redshift range selection. It follows that there is a significant overlap between the two samples with 65/110 (59%) of the COLA-N sources also being members of the RBGS.

Table 1 provides a summary of the COLA-N sample (for a similar table describing the southern sample see Corbett et al. 2002). The luminosity distance D_L given column 7 for each source was calculated in NED assuming the three attractor model of Mould et al. (2000) and the cosmological parameters derived from 5 year WMAP data (Hinshaw et al. 2009), i.e. $\Omega_m = 0.276$, $\Omega_v = 0.726$ and $H_o = 70.5$ kms^{-1}. Details on the calculation of Infra-red and radio luminosities presented in Table 1 are given in §3.3. Table 1 shows that most COLA sources have bolometric IR luminosities close to the boundary defining Luminous Infra-Red galaxies (at $L_{\rm IR}$=$10^{11}L_{\odot}$, Sanders & Mirabel (1996)) with a median IR bolometric luminosity for COLA-N of $10^{11.01}L_{\odot}$. All but one source has a bolometric IR luminosity in the range $10^{10.5} < L_{\rm IR}/L_{\odot} < 10^{11.7}$, the exception being the nearby ULIRG Arp 220.

Low resolution 1.4, 2.5 and 4.8 GHz continuum observations of COLA-S sources have been made using the Australia Telescope Compact Array (ATCA). These radio observations were complemented with high resolution single baseline 2.3 GHz snapshot observations obtained using the Australian Long Baseline Array (LBA). Optical spectroscopy for a large fraction of the southern sources was also obtained using the Dual Beam Spectrograph (DBS) on the 2.3 m telescope at the Mount Stromlo and Siding Springs Observatory. Detailed descriptions of the COLA-S radio and optical observations can be found in Corbett et al. (2002, 2003) respectively.

Corbett et al. (2002) detected 9 out of the 105 COLA-S galaxies in their LBA observations. Of these, 8 showed radio emission stronger than that predicted by the IR-radio correlation. Moreover 7 of the 14 sources with a total radio flux density more than 1σ above that predicted by the FIR-Radio correlation were LBA detections. Based on these results Corbett et al. (2002) concluded that sources detected with the LBA exhibited a statistically significant radio excess relative to the non-detections. This excess persisted even after the subtraction of the radio emission from the detected core implying the existence of associated AGN powered diffuse radio emission from structures larger than ∼15 pc.

The COLA-S optical data (Corbett et al. 2003) showed that in the southern sample the fraction of galaxies optically classified as Seyfert was ∼15%. Of these only 55% were detected with the LBA suggesting the there may be two populations of Seyferts, one population with extended radio structures and compact radio cores and the other without. In this paper we revisit these tentative conclusions in light of the larger number of long-baseline detected sources in COLA-N.

3. Observations

3.1. VLA Observations

Snapshot radio continuum observations for the COLA-N sources were obtained using the VLA at 4.8 GHz in two observing epochs each of 24 hours in length (see Table 2). Sources with $0^\circ < \delta < 30^\circ$ were observed on 1998/06/23 in the VLA BnA configuration, while sources with $\delta > 30^\circ$ were observed on 2003/07/19 in the A configuration. In addition, to ensure that all compact sources were observed with the A-array, 12 sources found to be compact at 4.8 GHz from the first epoch were re-observed in the second epoch. The data were reduced using AIPS in a standard manner. Radio maps of size $50'' \times 50''$ centered at the *IRAS* positions were produced for all the sources using natural weighting. Typical FWHM beam-sizes at 4.8 GHz were $\sim 0.4''$ and $0.9'' \times 0.4''$ for A and BnA configurations respectively. The typical rms noise levels were 75 μJy beam^{-1}

3.2. VLBI Observations

VLBI 4.8 GHz snapshot observations at data-rate 1 Gbit s^{-1} per station were conducted for the COLA North sample using the most sensitive telescopes available in the European VLBI Network (EVN). The first epoch on Feb 27/28th 2005 used Eb (Effelsberg), Wb (Westerbork) and Ar (Arecibo) for all sample sources within the declination range $10^\circ < \delta < 40^\circ$ (defined by the Ar zenith-distance restrictions and minimum elevation at the European stations) with ∼15 minutes of on-source time per target giving σ=25 μJy on the Ar–Eb baseline. The second epoch on May 6/7th

2005 used Eb, Wb and Jb1 (Jodrell Bank, Lovell telescope) for all the sources with $0^\circ < \delta < 10^\circ$ and $\delta > 40^\circ$ with $\sim$15 minutes of on-source time per target giving noise σ =56 μJy on the Eb–Jb1 baseline. Gaps in the schedule were filled by re-observing 21 sources from the first epoch. In both epochs strong nearby phase reference and amplitude calibrators (>500 mJy) were observed for 10 minutes every $\sim$1 hour. The Eb–Wb baseline (266 km) which is common to both epochs has a fringe spacing of 46.5 mas at 4.8 GHz which is similar to the 47.4 mas fringe-spacing of the ATCA–Tidbinbilla baseline (566 km) at 2.3 GHz used by Corbett et al. (2002) to observe the southern sample. Because of scheduling restrictions and bad data we only obtained useful VLBI observations for 90 sources.

AIPS was used for the initial data reduction and calibration stages with instrumental phase and delay being determined toward strong calibrators. Monitored system temperatures and gains were used to calibrate amplitudes. An adjustment of $\sim$30% was required on Jb1 to obtain consistent calibration on sources known to be unresolved from the VLBA calibrator database. Our final estimate is that quoted baseline flux densities are accurate to $\sim$15%.

Fringe fitting was performed in AIPS on all the calibrators and then these solutions were applied to the interleaved target source scans. After this we exported the data to our own software within which Delay–Rate maps were made for each baseline/target source. The size of these delay-rate maps were set such that a compact source would be detectable up to 20″ from the correlation position. Finally the Delay–Rate maps were transformed into RA–Dec offset maps relative to the phase center. These maps show *only* features which are smaller than the baseline fringe spacing (see Parra 2007). We adopted a detection threshold of 6 times the measured r.m.s. noise. The high sensitivity and small fringe spacing of the Eb–Ar baseline resulted in a very small uncertainty on the phase center offsets of the detections. These VLBI position offsets are shown as crosses on the corresponding VLA map in Figure 2

3.3. Archival Data Radio and IR data

In addition to our own radio data our analysis made use of source 1.4 GHz total flux densities taken from the *NVSS* catalog (Condon et al. 1998). Infra-red total flux densities were taken from the *IRAS* Point Source Catalog (Beichman et al. 1988). In order to calculate source infrared to radio (1.4 GHz) ratios ($q_{1.4}$) as defined by Helou et al. (1985) we calculated for each source an equivalent FIR flux density from $S_{\rm FIR} = 1.26 \times 10^{-14}(2.58 f_{60} + f_{100})/3.75 \times 10^{12}$ W m^{-2} Hz^{-1} where f_{60} and f_{100} are the cataloged 60 and 100 μm *IRAS* flux densities. For comparison with COLA-S and other data sets for each source a FIR spectral luminosity (see Table 1, column 9) was calculated assuming isotropic emission. Finally bolometric IR (8μm -1000μm) luminosities in solar units were calculated (see Table 1, column 7) from the IRAS flux densities using the relation given by Sanders & Mirabel (1996).

3.4. Optical spectroscopy observations

Optical spectroscopy observations were taken using the 60 inch CfA telescope at Mt Hopkins, Arizona between February and October 2001 using the FAST spectrograph. A slit width of 3″ was used, corresponding to 0.9 kpc at the median sample source distance. A grating of 300 lines/mm was used to disperse light between 4000 and 7000Å and gave a spectral resolution of 6Å. A single exposure of between 900 and 1200 seconds was made for each target. Spectrophotometric and smooth standards (often the same stars) were observed during each night and used to flux-calibrate and correct for atmospheric absorption features in the spectra. We were able to measure useful line ratios for 61% of the sample.

Data reduction was carried out in the standard manner using IRAF. The frames were de-biased and flat-fielded. Galaxy spectra were extracted using an aperture centered on the position of peak flux across the slit. If more than one peak was seen in the spatial direction a spectrum was extracted at the position of each peak. Sky-subtraction was then carried out and wavelength calibration done using an Ne-Ar arc lamp. The observations were then corrected for atmospheric extinction and flux calibrated using the spectrum of a spectrophotometric standard. Finally atmospheric absorption features in the target spectra were removed using the smooth spectrum standard observed at a similar airmass to the target.

The line fluxes were measured by fitting (mul-

TABLE 1
COLA NORTH SAMPLE

IRAS Name (1)	Other Name (2)	R.A. J2000 (3)	Decl. J2000 (4)	$V_{\rm Hel}$ [km s^{-1}] (5)	D_L [Mpc] (6)	log $L_{\rm IR}$ [$L_\odot$] (7)	log $L_{1.4}$ [W Hz^{-1}] (8)	log $L_{\rm FIR}$ [W Hz^{-1}] (9)	$q_{1.4}$ (10)
00005+2140	MRK334	00 03 09.74	21 57 36.46	6579	93.4	11.07	22.46	24.74	2.27
00073+2538	N23	00 09 53.58	25 55 26.40	4566	64.7	11.09	22.57	24.82	2.25
00506+7248		00 54 04.00	73 05 11.70	4706	69.3	11.49	22.82	25.21	2.40
00521+2858		00 54 50.27	29 14 47.60	4629	65.2	10.88	22.39	24.62	2.23
00548+4331	N317	00 57 40.58	43 47 32.30	5429	77.2	11.16	22.66	24.92	2.26
00555+7614		*00 59 15*	*76 30 52*	4739	70.1	10.91	22.53	24.66	2.13
01503+1227		01 52 59.52	12 42 27.90	4558	63.3	10.91	22.36	24.65	2.29
01519+3640		01 54 53.93	36 55 04.40	5621	79.2	11.02	22.14	24.74	2.60
01555+0250	ARP126	01 58 05.26	03 05 00.90	5431	75.6	10.94	22.47	24.68	2.20
01556+2507		01 58 30.63	25 21 36.90	4916	68.8	10.99	22.36	24.75	2.39
01579+5015		02 01 09.65	50 30 25.50	4875	69.5	10.85	22.29	24.55	2.26
02071+3857	N828	02 10 09.52	39 11 25.30	5374	75.8	11.33	22.85	25.07	2.22
02080+3725	N834	*02 11 01*	*37 39 58*	4593	64.7	10.95	22.49	24.69	2.20
02152+1418	N877	02 17 58.62	14 32 25.90	3913	54.2	10.98	22.58	24.74	2.17
02208+4744		02 24 08.00	47 58 10.68	4679	66.5	11.09	22.51	24.84	2.33

COLUMNS— (1): IRAS Name (from Point Source Calalog, excepting F07258+3357 which is taken from the Faint Source Catlog). (2): Other name. (3)-(4): Right Ascencion and Declination (from VLA observations, unless undetected in which case IRAS positions are given in italics). VLA positions are conservatively estimated to be accurate to $0.3''$ and IRAS positions to $20''$. (5): Heliocentric velocity (cz) from NED. (6): Luminosity distance (see Section 2). (7): FIR luminosity (see Section 3.3). (8): 1.4 GHz luminosity calculated from the NVSS catalog (Condon et al. 1998). (9): FIR spectral luminosity (see Section 3,3). (10): $q_\nu = \log(L_{\rm FIR}/L_{1.4})$. The full version of this table is given in Table 1 (Full Version).

TABLE 2
SUMMARY OF RADIO OBSERVATIONS

Date	Array	Frequency [GHz]	Beamsize[b] [mas]	Sources	Typical RMS [μJy beam^{-1}][d]
98/06/23	VLA BnA	4.9	900x400	$0^\circ < \delta \leq 30^\circ$	75
03/07/19	VLA A	4.9	400	$\delta > 30^\circ$ and CC [a]	75
05/02/27	Eb–Wb–Ar[c]	4.9	1.8	$10^\circ < \delta \leq 40^\circ$	25
05/05/06	Eb–Wb–Jb1[c]	4.9	18.1	$0^\circ < \delta \leq 10^\circ$ and $\delta > 40^\circ$	56

[a]CC=Sources known to be compact at 4.9 GHz from the first VLA epoch.

[b]For the VLA observations this is the typical FWHM of the restoring beam. For the VLBI observations this is the typical fringe spacing of the longest baseline.

[c]Eb=Effelsberg, Wb=Westerbork, Ar=Arecibo and Jb1=Jodrell Bank (Lovell). Baselines lengths are Eb–Wb=266 km, Eb–Jb1=699 km and Eb–Ar=6901 km.

[d]r.m.s noise has units of μJy beam^{-1} for VLA observations but for VLBI observations refers to noise on most sensitive baseline in μJy.

tiple) Gaussians to the emission lines using NGAUSSFIT in IRAF. The continuum flux was subtracted using a linear fit to small portions of the continuum either side of the emission line. The Hα (λ 6562Å) and [NII] doublet ($\lambda\lambda$ 6583, 6548Å) were often overlapping, in these cases line profiles were de-blended by simultaneously fitting a separate Gaussian for each line. When Hα was present in absorption as well as emission both the emission and absorption features were fitted simultaneously with Gaussians.

4. Results

4.1. Sample overall Radio/FIR ratios

In a FIR-selected sample of galaxies such as COLA, it is expected that in most sources star-formation will be the dominant mechanism powering the FIR emission. For such sources radio and FIR luminosities and flux densities are expected to be tightly correlated (see Condon 1992). The total 1.4 GHz and FIR luminosities for our sample are plotted in Figure 1-Left. Except for one outlier (3C84) which is unusually radio luminous, sources tightly follow the expected correlation. We calculated for each source the logarithmic ratio of flux densities $q_{1.4} = \log(S_{\rm FIR}/S_{1.4})$ as defined by Helou et al. (1985). Excluding 3C84, the mean value of $q_{1.4}$ is 2.34 ± 0.01 (and the median 2.31 ± 0.01) which is in good agreement with the mean $q_{1.4} = 2.34 \pm 0.01$ measured by Yun et al. (2001) from a sample of 1809 galaxies (solid line in Figure 1). In contrast the median value for COLA-S (Corbett et al. 2002) is $q_{1.4} = 2.43 \pm 0.03$ which is significantly (4σ) larger than the COLA-N median value.

To try to resolve the above discrepancy we compared *NVSS* and COLA fluxes for the 56 COLA South sources also contained in the *NVSS* catalog (i.e. those with $\delta \geq -40°$). We found *NVSS* flux densities for these sources which were 12% larger than those measured by Corbett et al. (2002), resulting in $q_{1.4} = 2.36 \pm 0.05$ for ATCA fluxes and 2.31 ± 0.04 for NVSS fluxes. It has been noted by Prandoni et al. (2000), Norris et al. (2006) and Kellermann et al. (2008) that for sources with flux densities $\lesssim 15$ mJy *NVSS* flux densities tend to be $\sim 10\%$ larger than ATCA measurements. Although COLA total flux densities are about a factor of two above this flux limit the effect is neither understood nor well-defined and so this scale difference may contribute to the apparent difference of median $q_{1.4}$. We conclude that the difference in $q_{1.4}$ between COLA-N and COLA-S is likely caused by (a) a $\sim$10% calibration difference for weak sources between NVSS and ATCA flux densities, combined with (b) a small number of sources at $\delta < -40°$ which have anomalously large values of $q_{1.4}$, perhaps simply because of small number statistics.

It remains unclear whether the likely $\sim$10% calibration difference between Northern and Southern hemispheres noted above for weak sources is a property of NVSS specifically or all VLA observations. Furthermore the 4.8 GHz measurements of galaxies made with the Bonn 100m single dish give $q_{4.8} = 2.71 \pm 0.03$ (Wunderlich et al. 1987), assuming a spectral index of 0.75 this then gives an estimated $q_{1.4} = 2.31 \pm 0.03$ close to the VLA value, supporting the idea that Northern hemisphere $q_{1.4}$ values are consistent with each other. Given the importance of sorting out the origin of radio flux scale differences between hemispheres it seems that dedicated simultaneous ATCA/VLA observations of sources with different flux densities should be made.

4.2. VLA 4.8 GHz Maps

The results of our VLA observations are summarized in Table 3. We successfully detected and mapped 95 out of the 110 observed sources. The 15 non-detections are probably large galaxies with a surface brightness too low to be detected with the VLA configuration used.

The images for the VLA detections are shown in Figure 2 and Figures 3.1–3.7 with the former showing sources which are also VLBI detections and the latter showing those that are VLBI non-detections. The images show a wide variety of morphologies. Following Neff & Hutchings (1992) we have classified the sources into four different morphological classes: Core (C), Core and Extensions (CE), Extended with no core (E) and Undetected (U) each class containing 28, 62, 5 and 15 sources respectively. There are two sources with clear ring structures, namely IRAS05091+0508 (NGC 1819) and 23488+1949 (NGC 7771), there are an additional four showing elongated linear structures typical of edge-on disks.

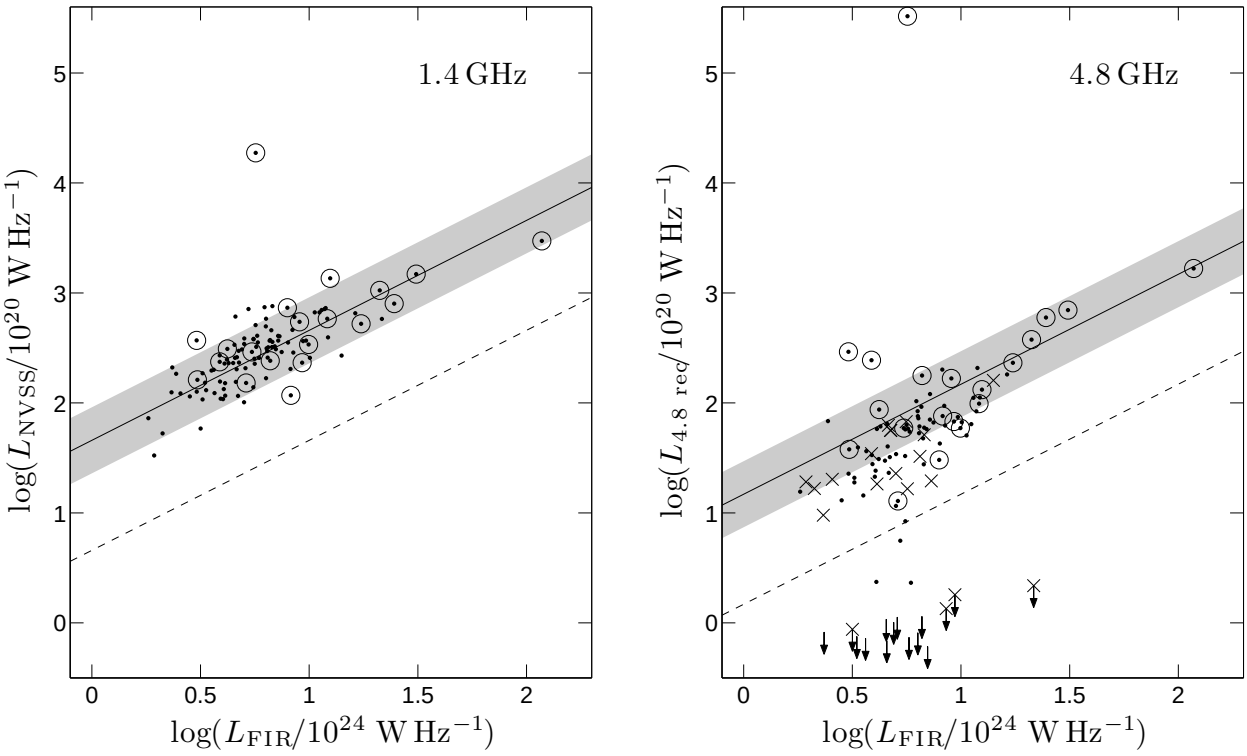

Fig. 1.— FIR to Radio correlation plots for the COLA North sample at 1.4 GHz and at 4.8 GHz. In both panels sources detected by VLBI are shown circled. Left: 1.4 GHz radio spectral luminosity calculated using *NVSS* fluxes versus FIR spectral luminosity $L_{\rm FIR}$ (see §3.3). Most of the COLA North sources are tightly clustered around the median $q_{1.4} = 2.34$ estimated for a sample of 1809 galaxies by Yun et al. (2001) which is shown by a solid line. Note on average that for the sample $L_{\rm FIR} = 1 \times 10^{25}$ WHz^{-1} corresponds to $L_{\rm IR} = 10^{11.25} L_{\odot}$. Right: 4.8 GHz spectral luminosity calculated using the recovered 4.8 GHz fluxes from our VLA maps (see §3.1) versus $L_{\rm FIR}$. Arrows indicate 5σ upper limits for the 15 sources not detected in these observations. Crosses indicate the 20 sources having no VLBI data. The median $q_{4.8} = 2.83$ measured by Wunderlich et al. (1987) from a sample of 99 normal spirals is shown by a solid line. In both panels, the gray area defines the region of ± 0.3 dex around the median and a dashed line is drawn at -1 dex.

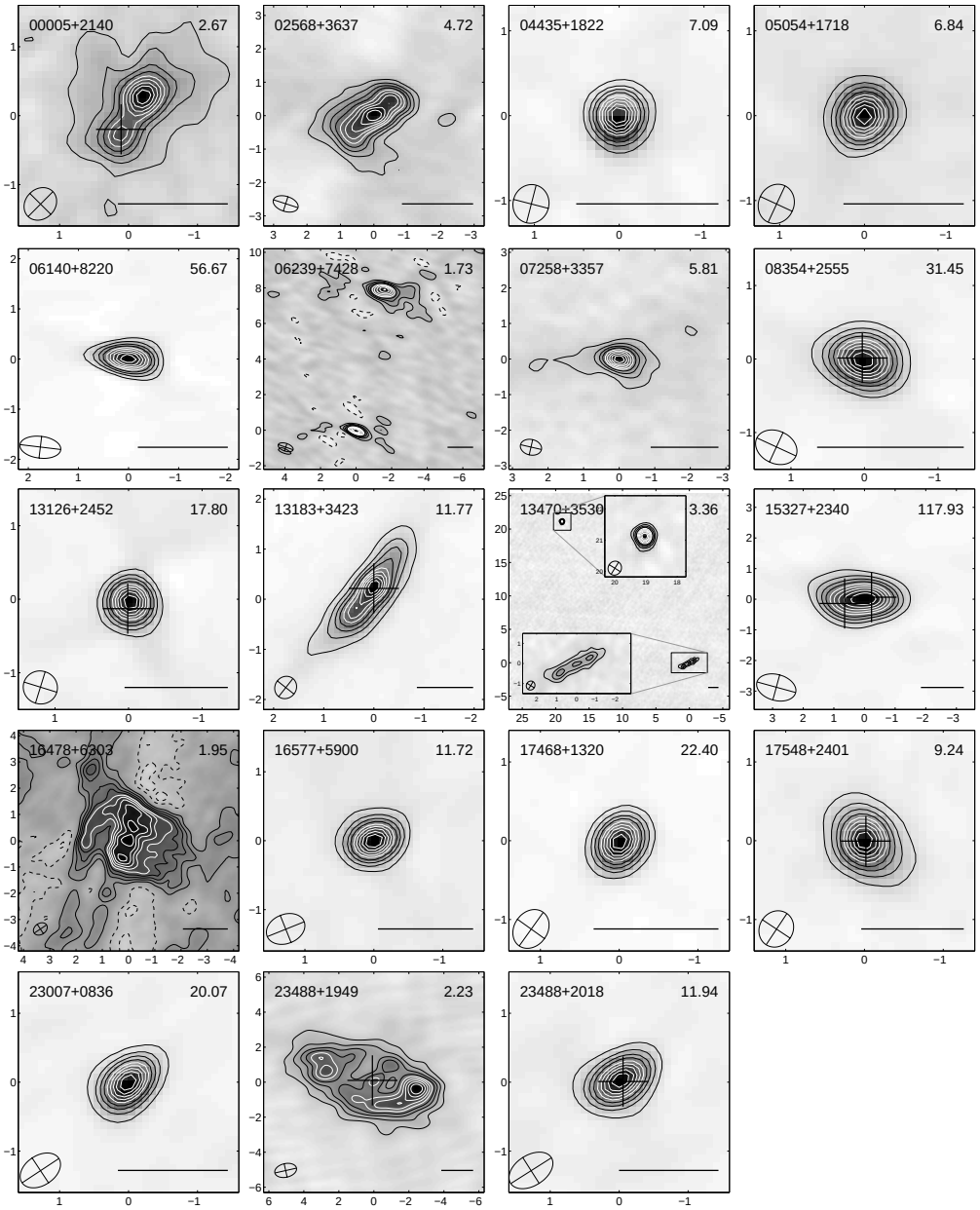

Fig. 2.— VLA 4.8 GHz naturally weighted maps for 19 of the 20 VLBI detected sources (the well known core-dominated source 031643+4119 (3C84) is omitted). VLA images of the sources undetected by VLBI are given in Figure 3.1–3.7. Shown are the highest resolution images of each source which in all cases come from A-array observations except for 15327+2340 (Arp220) and 23488+1949 which come from BnA observations. In 05336+5407 two features are detected 30″ apart, only the brighter more compact NW feature which contains the VLBI source is shown. In all of the figures the IRAS source name is indicated in the top left-corner. Peak brightness in mJy beam^{-1} is indicated in the top right corner. Black contours are drawn at 10, 20, 30 and 40% of the peak brightness. White contours are drawn at 50, 60, 70, 80 and 90% of the peak brightness. Negative contours are drawn with dashed lines at −10, −20, −30 and −40% of the peak brightness. A cross indicates the position of the VLBI core detections for those source having observations using the Eb–Ar baseline. Axes tick-marks are in arcseconds. The horizontal line on the bottom-right corner indicates 500 pc at the distance of the source.

Total recovered fluxes at 4.8 GHz ($S_{4.8\ \mathrm{total}}$) were obtained by integrating the flux over a region enclosed by the lowest reliable contour of radio emission. The median $q_{4.8} = \log(L_{\mathrm{FIR}}/L_{4.8\ \mathrm{tot}})$ obtained for the sample is 3.03 ± 0.05 which is significantly higher than the 2.71 ± 0.03 measured by

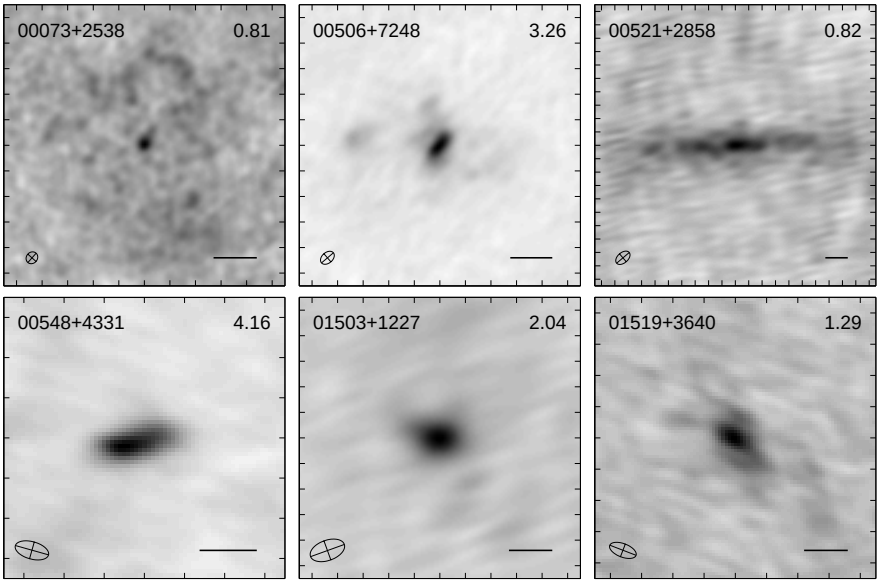

Fig. 3.1–3.7.— VLA 4.8 GHz naturally weighted maps for the VLA detected sources of the COLA North sample without VLBI detections. Maps for the VLBI detections are given in Figure 2. Column 2 in Table 3 gives the VLA array used, for sources observed in two arrays the higher resolution image is shown. IRAS names are indicated on the top-left corner of every panel. Peak brightness in mJy beam^{-1} is indicated on the top-right corner. Tick marks are separated by 1 arcsecond with the restoring beam shown at the bottom-left corner. The horizontal line at the bottom-right corner is 500 pc at the distance of the source. Only the first six images are shown here the remaining images can be found in the online version Figures 3.2 to 3.7.

Wunderlich et al. (1987) using single dish observations of a sample of 99 normal spirals. We conclude that we are on average resolving out $\sim$50% of the 4.8 GHz flux density. We note however that for those sources with compact central features the fraction of missing flux density is $\lesssim 20\%$.

4.3. VLBI Detections

We detect, on at least one VLBI baseline, 20 out of 90 sources observed. The measured flux densities on each baseline are given in Table 4. On the shortest Eb–Wb baseline (see Figure 4) the signal to noise ratio for most detections is generally significantly larger than the 6σ detection threshold (see Figure 4) while none detections are bounded to $<4\sigma$. It is notable that we obtain VLBI detections for 5 of the 6 sources with IR luminosities above $10^{11.4}\,L_{\odot}$. A histogram showing the VLBI detections and non-detections versus IR luminosity is presented in Figure 5-top which shows that the probability of detecting a VLBI core increases with IR luminosity.

Table 4 shows that there are 9 sources with simultaneous measurements on the Eb–Wb and Eb–Jb1 baselines. Of these, 7 have similar fluxes (within the noise) on these two baselines, the latter of which is $\sim$2.6 times longer than the first, showing that the VLBI component is unresolved.

Of the 14 sources with simultaneous Eb–Wb and Eb–Ar observations 9 are detected on the Eb–Ar baseline, but with significantly reduced flux density, indicating that the VLBI sources are resolved on the longest baseline. We estimate an angular size (see Table 4) by approximating the flux ratio between both baselines to that expected from a circular Gaussian (see Pearson 1999).

4.4. FIR/radio ratios of the VLBI Detections

Figure 1-left shows that the total 1.4 GHz VLA flux densities of our VLBI detected sources follow the FIR to radio correlation. There are 15/20 detections within ± 0.3 dex of the empirical line defined by Yun et al. (2001) (i.e. within

TABLE 3

RADIO AND OPTICAL OBSERVATIONS AND RESULTS

IRAS Name (1)	VLA Array (2)	VLA Morph (3)	$S_{4.8\ \mathrm{total}}$ (mJy) (4)	$q_{4.8}$ (5)	$S_{4.8\ \mathrm{comp}}$ (mJy) (6)	$\theta_M \times \theta_m$ [$'' \times ''$] (7)	$\log T_b$ [K] (8)	VLBI Epoch (9)	Optical Class (10)
00005+2140	BnA–A	CE	5.66	2.97	0.00	–	–	1*	S
00073+2538	BnA–A	C	18.40	2.85	1.23	0.45×0.22	2.63	1	C
00506+7248	A	CE	31.60	2.95	13.60	1.27×0.66	2.75	2	–
00521+2858	BnA	E	6.07	3.13	3.40	3.15×0.91	1.61	1	–
00548+4331	A	CE	13.21	2.95	13.11	1.51×0.41	2.87	2	–
00555+7614	A	U	–	–	–	–	–	2	–
01503+1227	BnA	CE	6.23	3.18	5.25	1.58×1.03	2.05	1	C
01519+3640	A	CE	4.38	3.23	3.92	1.13×0.74	2.21	1-2	C
01555+0250	BnA	CE	8.23	2.92	1.85	2.04×1.06	1.47	–	L
01556+2507	BnA	CE	11.16	2.95	7.37	1.32×1.02	2.28	1	H
01579+5015	A	CE	2.49	3.39	1.82	0.59×0.38	2.45	2	L
02071+3857	A	E	12.20	3.15	0.93	0.85×0.56	1.83	2	–
02080+3725	A	U	–	–	–	–	–	1-2	H
02152+1418	BnA	CE	2.39	3.82	1.34	1.49×0.94	1.52	1-2	–
02208+4744	A	CE	10.92	3.08	10.61	1.78×1.02	2.31	2	–
02253+1922	BnA	U	–	–	–	–	–	1-2	H

COLUMNS— (1): IRAS Name (2): VLA array(s) used (3): Morphology class of VLA 4.8GHz image. C-Compact, E-Extended, CE-Compact plus Extended, CER-Compact plus extended with ring, U-Undetected. (4): Recovered 4.8GHz flux density in VLA image. (5). Log of ratio of 4.8GHz recovered VLA flux density to FIR flux density. (6): Total flux density of gaussian fitted to brightest feature in VLA image (after removing VLBI component, hence zero indicates that brightest feature was dominated by the VLBI component). (7): Fitted gaussian major and minor axes to peak VLA feature (FWHM arcsec), Note for IRAS15327+2340 (Arp 220) these are for the western nucleus as taken from the literature (see Section 4.5). (7): Fitted gaussian major and minor axes to peak VLA feature (FWHM arcsec). (8): Peak 4.8GHz brightness temperature of gaussian component (see Section 4.5). Note if formally unresolved along one axis a 50mas FWHM was assumed along that axis). (9): VLBI Epoch(s) observed (asterisk indicates VLBI detection, see Table 4 for details). (10): Optical Class (see Section 4.6) with H=HII, S=Seyfert, L=LINER and C=Composite.

the grey region shown). Of the remainder two are just slightly above and two slightly below the ± 0.3 dex line. Only one source, 3C84, is significantly above the correlation. At 4.8 GHz a similar trend is observed with 14/20 detections located within ± 0.3 dex of the empirical line defined by Wunderlich et al. (1987). Consistent with the above results we find the median $q_{1.4}$ for the VLBI detections and non-detections to be indistinguishable (i.e. 2.30 ± 0.08 and 2.31 ± 0.02 respectively). Likewise if we omit 3C84 the mean of the VLBI detection is 2.33 ± 0.08 and of the non-detections is 2.32 ± 0.02. We can conclude that the data show that excepting 3C84 the total radio flux density is dominated by star-formation regardless of whether or not a VLBI core is present.

The above results appear to differ from those in COLA-S where a difference in median $q_{1.4}$ between VLBI detections and non-detections was claimed. From Table-3 of Corbett et al. (2002) the median $q_{1.4}$ value and its estimated one sigma error for the nine definite COLA-S VLBI detections was 2.07 ± 0.17 while for the VLBI non-detections it was 2.44 ± 0.03. The errors on theses estimates are calculated from the internal dispersion about the median $q_{1.4}$ for the two sub-samples as given in Corbett et al. (2002). We ascribe this apparent two sigma difference between the two sub-samples in the South as being due to the lower VLBI sensitivity in the South combined with the overall form of the $q_{1.4}$ distribution. This distribution has a tail of radio core-dominated, low $q_{1.4}$ sources (such as 3C84 in the North and NGC5793 in the South) which are easily VLBI detected plus weaker VLBI cores in galaxies whose radio emission is star-formation dominated. The lower sensitivity VLBI observations in the South contain a larger fraction of the former class of source which reduces the estimated $q_{1.4}$ of VLBI detection compared to non-detections. Specifically in the South 4 out of 9 VLBI detected sources have $q_{1.4} \lesssim 2$ while the fraction is only 3 out of 20 in the North. Because low $q_{1.4}$ sources comprise almost half of the VLBI detected sample in the South they can bias the median $q_{1.4}$ while in contrast in the North such outlier sources have negligible effect.

TABLE 4
VLBI RESULTS

COLA name (1)	Other name (2)	Eb–Wb [mJy] (3)	Eb–Jb1 [mJy] (4)	Eb–Ar [mJy] (5)	Angular Size [mas] (6)	Linear Size [pc] (7)	Optical Class (8)
00005+2140	Mrk 334	1.67 (0.15)	—	1.02 (0.03)	0.68	0.29	S
02568+3637		1.61 (0.14)	1.92 (0.16)	—			S
03164+4119	3C84			15500(0.02)			L
04435+1822		3.32 (0.14)	—	3.10 (0.03)	0.25	0.07	H
05054+1718		1.64 (0.18)	—	< 0.20	>1.41	>0.50	S
06140+8220		4.12 (0.32)	—	—			-
06239+7428		—	1.51 (0.19)	—			-
F07258+3357	N2388	1.38 (0.18)	1.26 (0.14)	< 0.20	>1.35	>0.35	H
08354+2555	Arp 243	2.03 (0.10)	—	0.27 (0.02)	1.38	0.49	-
13126+2452		1.38 (0.17)	—	0.88 (0.04)	0.65	0.16	-
13183+3423	Arp 193	2.17 (0.17)	3.85 (0.15)	0.70 (0.04)	1.03	0.46	C
13470+3530		1.79 (0.11)	5.64 (0.16)	< 0.18	>1.47	>0.48	-
15327+2340	Arp 220	4.37 (0.17)	—	2.68 (0.04)	0.40	0.14	L
			—	1.02 (0.04)			
16478+6303	N6247	2.60 (0.12)	< 0.82	—			-
16577+5900	Arp 293	6.11 (0.27)	5.36 (0.17)	—			C
17468+1320		8.33 (0.21)	5.31 (0.13)	< 0.25	>1.82	>0.57	-
17548+2401		4.45 (0.20)	—	0.39 (0.04)	1.52	0.58	L
23007+0836	N7469	5.12 (0.22)	6.32 (0.15)	—			S
23488+1949	N7771	< 1.14	—	0.33 (0.04)	<1.08	<0.28	L
23488+2018	Mrk 331	5.02 (0.21)	4.92 (0.13)	0.30 (0.04)	1.63	0.57	C

NOTE.—COLUMNS — (1): IRAS Name (from Point Source Calalog, excepting F07258+3357 which is taken from the Faint Source Catlog). (2): Other name. (3)-(5): VLBI flux and 1σ uncertainty (in brackets) obtained from the peak in the Delay–Rate map. Upper limits for the non-detections are indicated at 5σ. A dash is shown for sources not observed at that baseline. For IRAS15327+2340 (Arp 220) on the longer baselines the two rows give results for the West and East nuclei respectively. (6): FWHM of a circular Gaussian source fitting the flux ratio between the Eb–Wb and Eb–Ar baselines (see §4.3). Sources with flux upper limits on the Eb–Ar have consequently size lower limits. (7): Corresponding fitted Gaussian FWHM linear sizes. (8): Optical Class (see Section 4.6) with H=HII, S=Seyfert, L=LINER and C=Composite; a dash indicates no optical line data.

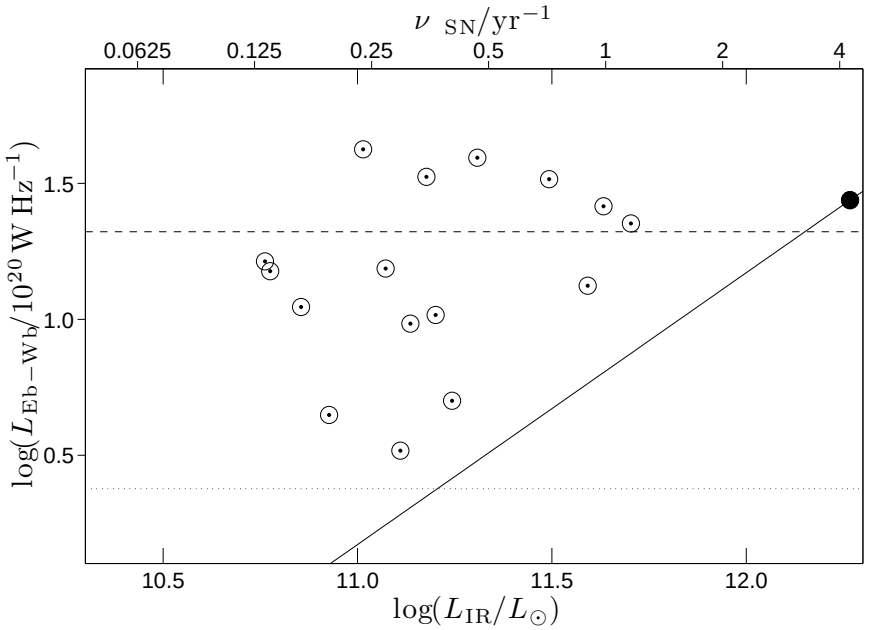

Fig. 4.— Radio spectral luminosity at 4.8 GHz on the Eb–Wb baseline for VLBI detected sources (excluding 3C84) versus IR luminosity. The source Arp 220 is shown as a filled circle. The scale on the upper horizontal axis indicates the core-collapse supernova rate $\nu_{\rm SN}$ estimated from the IR luminosity using the formula in van Buren & Greenhouse (1994) (after applying a small FIR to IR luminosity correction). The luminosity at maximum light measured for the powerful Type IIn SN1986J is indicated with a horizontal dashed line at $2.1{\times}10^{21}\,{\rm W\,Hz^{-1}}$. The diagonal line represents the spectral luminosity detected on the Eb–Wb baseline for Arp 220 scaled by IR luminosity. The lower horizontal dotted line indicates our typical 6σ=780 μJy detection threshold on this baseline at the median distance of the COLA sample.

4.5. Relation Between VLA and VLBI Sources

Visual inspection of the VLA radio maps indicates a bias for VLBI detections to be in sources with compact structure and high peak brightness (see Figure 2). This is confirmed in terms of VLBI detection rate versus morphology class (see §4.2) . Amongst the VLBI observed sources there are 13/27 detections of class C, 6/48 of class CE and 1/5 of class E. We do not detect any class U source. This result was confirmed by plotting VLA visibility amplitude versus *uv* distance. The majority of VLBI detections were indeed found in sources with compact, but not unresolved, arcsec-scale structures. The size of these structures was estimated by subtracting an unresolved source equivalent to the VLBI detection from the brightest component in each VLA map and then fitting a Gaussian to the difference.

In two cases (00005+2140 and 06239+7428) the VLBI core subtraction removed all the flux density implying that the brightest VLA component was caused completely by the VLBI source itself. We consider these two sources together with 03164+4119 (3C84) to be *VLBI core-dominated sources* and omit them from the subsequent analysis. For the rest of the sources the task JMFIT was used to fit a Gaussian within a tight box containing the remaining feature. For the vast majority of sources in classes C and CE with a clear compact component there was no ambiguity in the Gaussian fitting, i.e., the results of the fits were the same regardless of the size of the fitting box. For sources in class E the size estimates were found to vary by up to a factor of $\sim$2 depending on the chosen box. However in all such cases the fitted sizes were large ($\gtrsim 2''$). The resulting component flux densities and major and minor axes θ_M and θ_m are listed in columns 6 and 7 of Table 3.

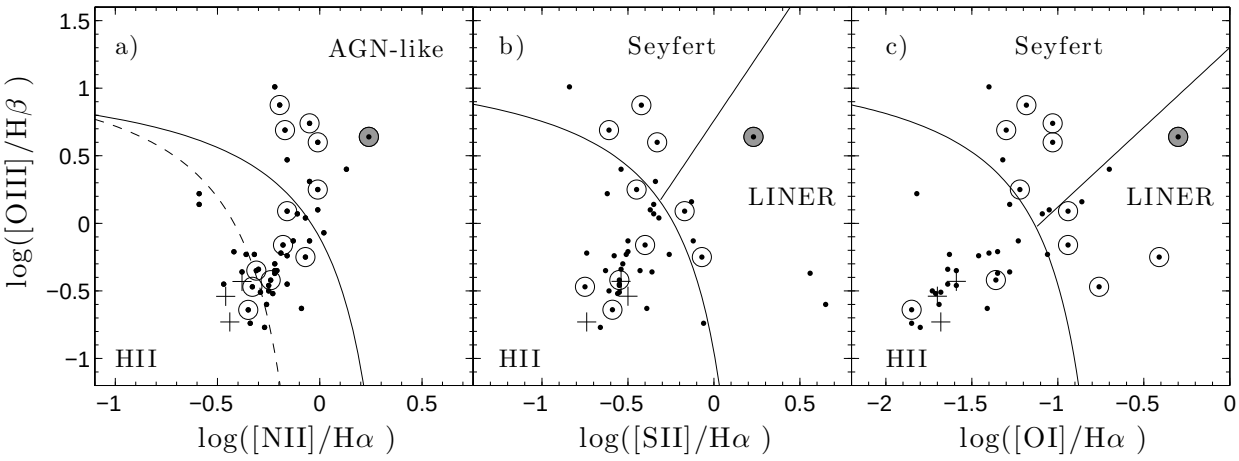

Fig. 6.— Optical-line diagnostic diagrams ("BPT" diagrams) for the COLA-N sources that are both VLBI observed and have available optical line data. Dots indicate VLA detected sources and crosses those undetected by the VLA. VLBI detected sources are shown circled. **a)** [NII]/Hα v/s [OIII]/Hβ diagram. The solid and dashed curves are respectively the theoretical Kewley et al. (2001) extreme starburst line and the Kauffmann et al. (2003) empirical line for star-forming galaxies. Sources that lie between the two curves are classified as composite Starburst/AGN. **b)** [SII]/Hα v/s [OIII]/Hβ diagram **c)** [OI]/Hα v/s [OIII]/Hβ diagram. In the latter two panels the solid curved line is the extreme starburst line from Kewley et al. (2001) and the straight diagonal line separates Seyferts from LINERS (Kewley et al. 2006). Note that for some sources not all line ratios are plotted because some lines were not detected. The shaded VLBI detected source is 15327+2340 (Arp220).

Peak brightness temperatures T_b at 4.8 GHz for the compact VLA structures were calculated using the relation $T_b \simeq 35{\times}(S_{4.8\,\mathrm{peak}})(\theta_M{\times}\theta_m)^{-1}$ K° (Column 8 in Table 3). In a few sources the fitted deconvolved minor axis was zero, in these cases its size was set to 50 mas which was equal to the smallest size found in other sources.

Uniquely amongst sources with compact structure we did not collect any VLA A-array data for the well known ULIRG source 15327+2340 (Arp220). In order to treat this source in a similar way to the rest we give in Table 3 radio component properties from the literature for the brighter western nucleus (sizes from Condon et al. (1991) with flux densities scaled to 5 GHz using the spectral index of Rovilos et al. (2003)).

As can be seen from Figure 5 (bottom panel) VLBI detections seem to be strongly correlated with those sources whose VLA fitted components (after removing any VLBI contribution) have the highest T_b. VLBI detectability is less strongly correlated with large L_{IR} (top panel). Two sided Kolmogorov-Smirnov tests comparing the distribution of VLBI detected and non-detected sources in L_{IR} and T_b in each case rejects the hypothesis that VLBI/non-VLBI sources are drawn from the same population at probability levels of $P = 0.82$ and $P = 0.98$ respectively. This result demonstrates that the stronger correlation for VLBI detectability is with T_b rather than with L_{IR}.

4.6. Optical Spectroscopy Classifications

To classify sources based on their line ratios from our optical spectroscopy observations (see §3.4) we used the method of Kewley et al. (2006). This scheme first classifies sources into HII galaxies, AGN/star-formation composites and pure AGN based on a mixture of theoretical (*maximal starburst,* Kewley et al. 2001) and empirical line-ratio boundaries (Kauffmann et al. 2003) delineating pure star-forming galaxies. These boundaries are shown respectively as solid and dashed curves delimiting the bottom left corners of the diagnostic line ratio diagrams in Figure 6. HII galaxies (class H) are to the left and below all the curves including the dashed line in Figure 6a. Composite

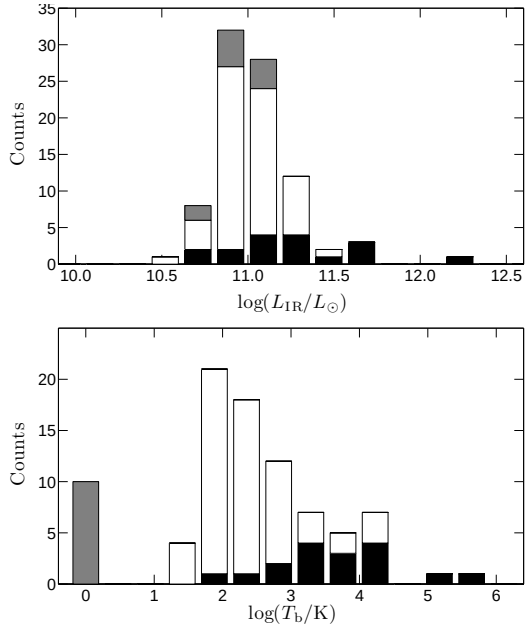

Fig. 5.— Histograms of IR luminosity (top panel) and peak brightness temperature of VLA scale radio component (bottom panel) for VLBI observed sources. In both panels VLBI detections are shown black. VLBI non-detections for sources respectively detected and undetected by the VLA are shown white and grey respectively. The brightness temperature in the bottom panel is calculated after subtraction of the VLBI component from the VLA map (see §4.2). Note for ease of comparison the three VLBI core-dominated detections (i.e 00005+2140, 03164+4119, 06239+7428) are not plotted in either panel. A much stronger correlation between VLBI detection and high brightness temperature VLA scale emission is found than with IR luminosity (see Section 4.5 and also Fig 8)

sources (class C) lie between the solid and dashed lines in the [NII]/Hα diagram and AGN are above and to the right of the curves in all diagrams. The AGN population is further divided between Seyfert (class S) or LINER (class L) using the [SII]/Hα and [OI]/Hα diagnostic diagrams and the empirical results of Kewley et al. (2006) who found two well defined populations tracing different position angles on these diagrams. For a significant number of our sources either the [SII] or [OI] lines were not detected. In order to increase the number of detections we therefore used the same *2-of-3* criterion for classification as Yuan et al. (2010) whereby if there was no data for a given line ratio or if one diagram gave a classification inconsistent with the other two we chose the classification given by the majority of the diagrams.

Our available optical data allowed for the classification of 66 sources as summarized in column 10 of Table 3. The fraction of different classifications agrees well with that found amongst sources of similar luminosity by f Yuan et al. (2010). For the subset of sources observed by VLBI the compact radio core detection rates for each optical category are; Seyferts 4/8 (50%), LINERS 4/6 (66 %), Composite 3/20 (15%) and HII 2/15 (14%). These VLBI detection fractions are broadly consistent with the idea that VLBI cores trace AGN activity since the detection fraction is largest amongst AGN optical types (see §5.4).

5. Discussion

5.1. Nature of Detected VLBI Sources

The primary objective of our VLBI observations was to detect compact cores indicating AGN activity. Here we discuss whether our 20 VLBI detections can be taken as unambiguous signs of AGN activity or whether they might be confused by the high spatial frequency tail of arcsecond scale diffuse emission, radio supernovae (SNe), or supernova remnants (SNRs).

5.1.1. VLBI Brightness Temperature and Diffuse Starburst Emission

Could the VLBI detections be due to spatial substructure within the general ISM starburst-powered radio emission? As noted in §4.5 the flux densities on the Eb–Wb and Eb–Jb1 baselines are usually comparable so implying a source size less

than about half of the Eb–Jb1 fringe spacing, i.e. $\lesssim$10 mas. A typical VLBI detection flux density of $\sim$3 mJy would then imply a brightness temperature of at least $10^{6.2}$ K. Even larger brightness temperatures are found on the Eb–Ar baseline where sub-milliarcsecond sizes imply brightness temperatures of $\gtrsim 10^8$ K. These high brightness temperatures are inconsistent with star-formation powered synchrotron emission which is predicted to have brightness temperatures of $\lesssim 10^5$ K (Condon et al. 1991).

Given that we only have fringe detections on single baselines it is possible that such detections (especially on the Eb-Jb1 baseline) could be due to star-formation powered radio emission combined with an unusual source brightness distribution. One such distribution would be a thin rectangle with its small dimension < 10 mas along the direction of the fringe spacing; this would however require both unusual brightness distributions and chance alignments in position angle in a number of sources to affect our results. A second such distribution would be one with order 100% amplitude fluctuations of 10^5 K brightness on scales < 10 mas over a region of order 1000 mas in diameter, giving large r.m.s visibilities of the same size on Eb-Wb and Eb-Jb1. The ratio of detected visibilities on these two baselines seems too close to unity to be explained by such a random model. Additionally such a brightness distribution seems very unlikely, one would instead expect larger fluctuations as we go to larger separations within the source giving rise to larger r.m.s visibilities on the shorter baseline. This is what is in fact observed in Arp 220. Taking the data of Parra et al. (2007) and removing the effect of the compact sources we detect the diffuse emission on Eb-Wb but not on the Eb-Jb1 baseline. Since Arp 220 is brighter and more compact than other COLA sources it seems unlikely that the Eb-Jb1 detections in these can be due to randomly fluctuating diffuse 10^5 K emission.

5.1.2. Compact Sources in Arp 220

For the case of Arp 220 (15327+2340) most of the flux density detected in our VLBI snapshot observations clearly comes from non-AGN activity. This galaxy has been known for many years (Smith et al. 1998; Lonsdale et al. 2006; Parra et al. 2007) to harbor multiple compact radio sources consistent with a mixed population of luminous radio supernova remnants (SNRs, interacting with the ISM) and supernovae (SNe, interacting with progenitor winds). Arp 220 is however a very unusual source within the COLA sample being by far its most IR luminous object. It follows that a confirmed SNR/SNe origin for the VLBI snapshot fringes in Arp 220 does not necessarily imply that the same explanation is valid for the rest of the VLBI detections. The diagonal line in Figure 4 shows the Eb–Wb spectral luminosity of Arp 220 scaled linearly with $L_{\rm IR}$ and demonstrates that if the VLBI contribution from SNR/SNe scales linearly with star-formation rate then these cannot explain the VLBI detections. In the next subsections we discuss in more detail whether SNRs and SNe can in fact explain the VLBI detections.

5.1.3. Supernova Remnant Origin

Chomiuk & Wilcots (2009) find in their study of the radio luminosity function of SNRs in nearby normal and starburst galaxies a constant power law exponent and a scaling factor proportional to SFR. They also find both theoretically and empirically that the luminosity of the brightest SNR in each galaxy scales linearly with the SFR. Since even on our shortest VLBI baseline bright SNRs will be separated by several fringe spacings their expected contribution to the correlated VLBI flux density will be an incoherent sum of all the SNR flux densities. This incoherent sum will however, because of the constant slope SNR luminosity function found by Chomiuk & Wilcots (2009) simply be some multiple of the brightest SNR flux density. Since this latter quantity is linearly correlated with SFR we expect the total observed VLBI signal due to SNRs to also linearly scale with SFR. Since about half of the flux density seen on the Eb–Wb baseline for Arp 220 comes from SNR a VLBI contribution which lies a factor of two below the diagonal line shown in Figure 4 is therefore expected; in all cases this lies below the luminosity of the detected VLBI cores.

In fact estimating the SNR contribution to VLBI flux density in COLA galaxies by scaling Arp 220 by L_{IR} as described above probably results in an overestimate of the SNR contribution for COLA galaxies. This is because Chomiuk & Wilcots (2009) find that although the SNR luminosity function in Arp 220 has the same

slope as in other galaxies the scaling factor between SNR brightness and SFR is larger (possibly because of the very high gas density in Arp220). The true VLBI SNR contribution in COLA galaxies although having the same linear slope as drawn in Figure 4 therefore likely passes below the Arp 220 point; because this source is over-luminous in SNR for its SFR.

5.1.4. Radio Supernova Origin

A difficulty for calculating the possible contribution of radio SNe to our detected VLBI flux density is that unlike the case for radio SNR no well defined radio SNe luminosity functions have been published. It is clear however that only the most luminous Type Ic or Type IIn optical classes (Chevalier 2006) would be detectable at the distance of COLA galaxies. The most powerful Type Ic objects are often associated with γ-ray bursts and have rapid rise and decay times. The slightly weaker Type IIn SNe are much longer lived and hence more likely to be detected. Optically about 4% of core-collapse SNe are of Type IIn (Smartt et al. 2009) however even these show a wide range in radio luminosity. For instance all of the six IIn's observed by van Dyk et al. (1996) were undetected in the radio with 4.8 GHz spectral luminosity $<1.4\times10^{19}\,\mathrm{W\,Hz^{-1}}$. The likely Type IIn's in Arp 220 (Parra et al. 2007) have spectral luminosity of $\sim 4\times10^{20}\,\mathrm{W\,Hz^{-1}}$. The most radio luminous Type IIn so far detected ($2\times10^{21}\,\mathrm{W\,Hz^{-1}}$ at 4.8 GHz) is SN1986J in NGC 891 (Rupen et al. 1987). Sources close to this maximum seem however to be rare. Considering the number of optically identified Type IIn's searched in the radio (see Chandra et al. 2009, and references therein) in normal galactic disks we can estimate that at most one in ten Type IIn's (or 0.4% of all core collapse SNe) reaches to within a factor of two of the SN1986J radio luminosity.

Amongst COLA VLBI detections there are six objects other than Arp 220 with luminosities above that of SN1986J at maximum light (i.e. above the dashed line in Figure 4). A single RSNe origin seems to be ruled out for these objects and we are forced to consider models consisting of two or more extremely luminous objects. Such SN1986J-like objects stay within a factor of two of their peak 4.8 GHz luminosity for $\sim$5 years and host galaxies of these VLBI detections have total supernova rates of order $0.5\,\mathrm{year^{-1}}$. If 0.4% of core collapse are SN1986J-like, then we expect 0.01 such objects on average per COLA galaxy. The probability of getting just one example of two or more such luminous objects in a galaxy within our whole sample is thus only 1.5%.

Figure 4 shows 7 VLBI detections at $\sim1\times10^{20}\,\mathrm{W\,Hz^{-1}}$ that could potentially be explained as single SN1986J-like objects observed when above 50% of maximum light. Assuming the same radio luminous SNe lifetimes and fractions as before and typical SFRs of this group of $\sim0.25\,\mathrm{year^{-1}}$ there should only be 0.5 such objects in the whole sample. Finally there are three VLBI detections at $\sim0.6\times10^{20}\,\mathrm{W\,Hz^{-1}}$, it is possible that one of these objects could be a SNe, though without a detailed radio SN luminosity function it is hard to make any definite statements.

A general argument that suggests that the vast majority of our VLBI detections are not explained by SN comes from the fact (see §4.3) that all our VLBI detections are well above our detection limit. If the origin of the VLBI detections were single or multiple RSNe such a gap in luminosity between our weakest detection and the sensitivity limit is hard to explain. A single RSNe spends a much longer period at low luminosities than at high, and intrinsically weaker SNe are more common than strong ones, so one would expect many more detections just above the detection cutoff than are observed.

We conclude that, while one or two of the less luminous detections could be caused by radio SNe, the vast majority of our VLBI detections cannot and must instead be AGN powered.

5.2. Nature of Extended Radio emission

For most VLBI detected COLA sources (17/20), a large fraction of the total radio flux density arises from several 100 pc scale structures seen in the VLA maps. As noted in §4.1 the total flux densities of nearly all COLA sources, including both VLBI detections and non-detections (see §4.4 and Figure 1), closely follows the FIR to radio correlation at both 1.4 and 4.8 GHz. This result indicates that most of the radio emission recovered in the VLA maps is powered by star formation activity. It is known from observations of the starbursts in M82 and Arp 220 that the associated star for-

mation induced compact emission from SNR and SNe is just a few percent (Lonsdale et al. 2006) of the total diffuse component radio emission; hence there is no contradiction between star-formation being the main power source for the total radio emission and our conclusion that it does not provide enough correlated flux density to explain the VLBI detections.

5.3. Nature of integrated IR emission

Figure 7 shows a IR color–color diagram for the 90 sources with VLBI observations in the COLA North sample. Any position on this diagram can be reached by a linear combination of starburst temperature, AGN and reddening (Kewley et al. 2000). It is therefore impossible to unambiguously estimate the proportions in which these ingredients are combined. However, most of the sources in the sample appear to follow the line traced by blackbodies of progressively increasing temperatures (i.e. the starburst line) with a scatter apparently increasing with temperature suggesting a larger AGN contribution to the IR energy budget in warm starbursts. The overall scatter of the COLA sample is however much smaller than that observed by Rush et al. (1993) in their sample of optically selected Seyferts. We therefore argue that for most sources in our sample that their IR emission is mostly powered by starburst activity with any AGN contribution being energetically unimportant.

All 10 VLA non-detections (see §4.2) with VLBI data are clustered near the cold end of the starburst line (crosses in Figure 7). As discussed in §4.2 these are likely to be large sources whose relatively large FIR luminosity is not due to concentrated nuclear starburst activity but is instead caused by the aggregation of normal star forming regions spread over their large galactic disks.

5.4. Comparison of optical and radio source classifications

As discussed in §4.6 we find that the fraction of VLBI detections in AGN-like optical types is substantially higher than in HII type galaxies, supporting the interpretation that VLBI detections indicate AGN activity. We find however no one-to-one correspondence between the optical classification and VLBI detection. The fact that half of the observed Seyfert sources (4/8) were not detected by VLBI supports the result of Corbett et al. (2003) who found observationally two classes of Seyferts with and without detectable VLBI radio cores. This could simply be an artifact of our limited VLBI sensitivity or it could mean that there are physically two classes of Seyfert with different degrees of radio-loudness. The relatively high VLBI detection rate of LINER sources (4/6) is consistent with models in which this class is usually AGN powered (Kewley et al. 2006) although it is clear that in some sources LINER-like spectra can arise in shocks, i.e. for the case of Arp 220 (Arribas et al. 2001). The relatively low incidence of VLBI detections in HII galaxies (2/15) suggests that cases of completely optically obscured AGN are rare. Combining the VLBI and optical results we find the overall incidence of AGN activity to be high. If we add the four non-VLBI detected Seyferts to the 19 VLBI detections (excluding Arp 220) we get a minimum fraction of sources containing AGN of 22/90 (25%).

5.5. Implications for the AGN starburst connection

An interesting correlation found in the present work is that between the presence of a VLBI detection and of high brightness arcsecond-scale radio emission (see §4.5 and Figure 5). In §5.1 we argued that VLBI detections are due to AGN activity rather than SNe or SNRs. In §5.2 we further argued that the extended radio emission seen with the VLA is due to star formation. Taken together these results imply a strong connection between AGN activity and the presence of a compact starburst.

A significant body of evidence in favor of a strong starburst/AGN connection has been accumulating in recent years. In nearby AGN evidence is seen for for nuclear post-starburst stellar populations of age $\sim 10^6$–10^8 year (Davies et al. 2007) suggesting a possible evolutionary connection with nuclear starbursts preceding AGN activity (see also Heckman 2008). There are however also many individual examples of concurrent starburst/AGN activity (e.g. Fathi et al. 2006). The present paper has found evidence linking AGN activity with concurrent compact starbursts in FIR selected sources and it is interesting to consider possible physical interpretations of this result.

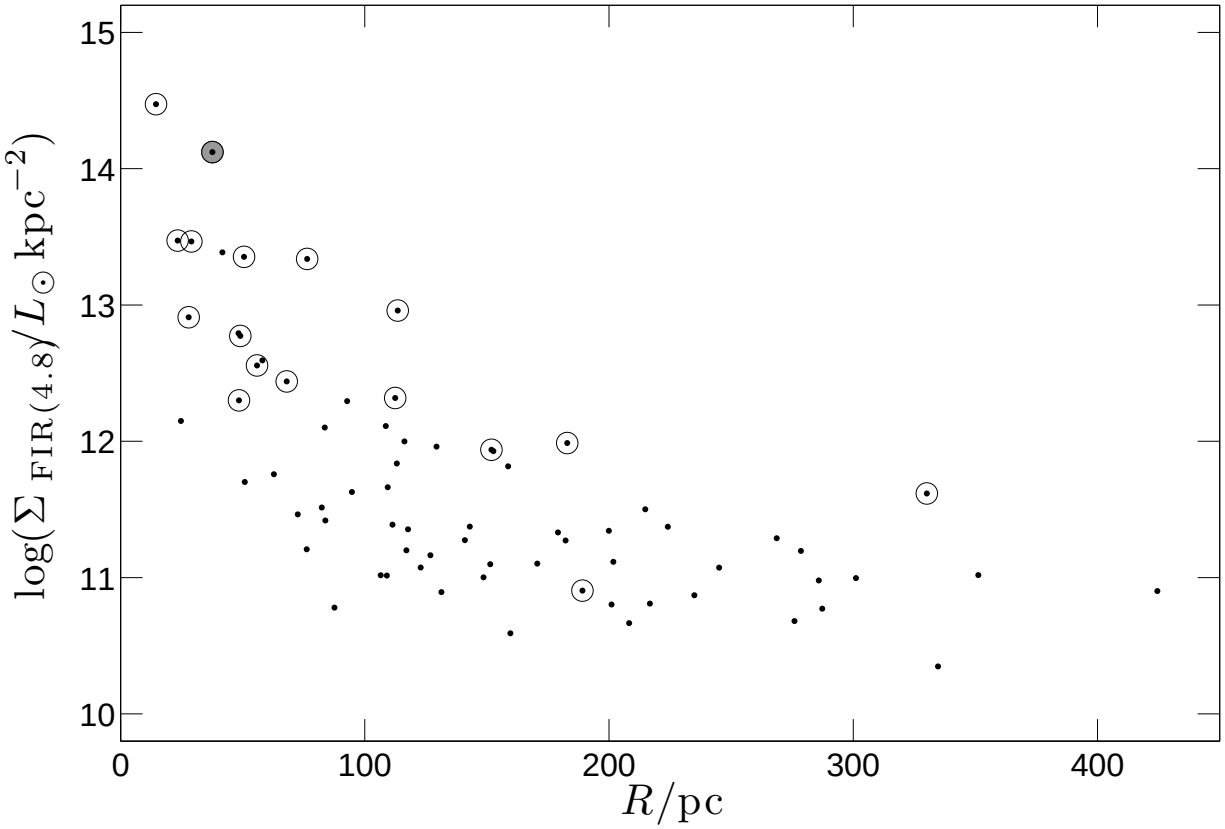

Fig. 8.— Starburst FIR equivalent brightness $\Sigma_{\rm FIR(4.8)}$ versus central starburst component radius R for sources both imaged by the VLA and observed by VLBI. VLBI detections are indicated by a circle with Arp 220 emphasized as a filled circle. This diagram duplicates a similar one in Thompson et al. (2005) for more luminous IR galaxies. In this plot $\Sigma_{\rm FIR(4.8)} = L_{\rm FIR(4.8)}/A_{\rm radio}$ where $L_{\rm FIR(4.8)}$ is the equivalent starburst FIR spectral luminosity estimated from the 4.8 GHz data and $A_{\rm radio}$ is the area of the central starburst source. $L_{\rm FIR(4.8)}$ is calculated by transforming the 4.8 GHz spectral luminosity of the brightest VLA component $L_{\rm 4.8peak}$ to an equivalent FIR spectral luminosity using the FIR-radio correlation.

.

The Eddington-limited starbursts discussed by Thompson et al. (2005), which can also feed central AGN, are predicted to have central peak bolometric brightness of $10^{13}\,L_\odot\,{\rm kpc}^{-2}$ consistent with the luminous compact starbursts from Condon et al. (1991). Figure 8 plots the estimated FIR surface brightness versus fitted size for the arcsecond-scale radio structures for our COLA sources, matching Figure 4 of Thompson et al. (2005). We find that our VLBI sources are mostly detected in sources with bolometric brightness approaching or around $10^{13}\,L_\odot\,{\rm kpc}^{-2}$ which coincides with values predicted for Eddington-limited starbursts.

Thompson et al. (2005) also argued for two separate modes by which such compact starbursts can feed a central black hole, supplying either $0.1 M_\odot{\rm year}^{-1}$ or $4 M_\odot{\rm year}^{-1}$ depending on whether the gas supply rate at several hundred parsec radius is smaller or larger than $220 M_\odot{\rm year}^{-1}$. The rest of this mass is converted into stars. Since the star formation rates of COLA sources are $\ll 220\ M_\odot{\rm year}^{-1}$ the lower black hole supply rate applies. Assuming an efficiency of 10% this supply rate translates into an AGN bolometric luminosity of $1.5{\rm x}10^{11} L_\odot$ which is comparable to the IR luminosities of the COLA galaxies with VLBI detections. Such a high AGN luminosity,

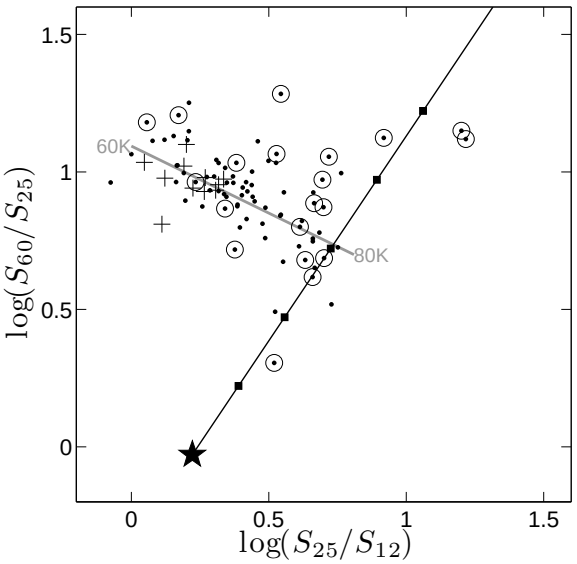

Fig. 7.— IR color-color diagram for COLA North sources observed by VLBI. VLBI detections are indicated with open circles and VLA non detections as crosses. The gray line is traced by blackbodies of temperatures progressing from 60 to 80 K from the left. The black line is a reddening line starting from the average warm Seyfert 1 nucleus (indicated by a star). Squares over this line are located at $\tau_{25\mu m}$=1, 2, 3, 4 and 5 (see Dopita et al. 1998).

which would mostly emerge in the IR, is inconsistent with the fact that COLA sources lie on the FIR-radio correlation and have IR colors typically found in starburst powered sources (see 5.3). We can speculate that a constant fraction of gas supplied to the black hole might be lost to winds or jets formed close to the black hole event horizon, thus reducing the AGN bolometric luminosity. The detected core radio emission would be generated at the base of these jets (Falcke & Biermann 1995). The starburst regulation of the gas supply would ensure that these jets had similar mass outflow rates and mechanical luminosities therefore explaining the relatively narrow range of radio luminosity of our VLBI detections.

The high incidence we find of AGN activity in compact high brightness starbursts (i.e. VLBI detections in 13/18 sources with specific star-formation rates $>10^{12}\,L_{\odot}\,\mathrm{kpc}^{-2}$, see Figure 8) suggests only a short interval between the triggering of such starbursts and the onset of AGN activity. In contrast Davies et al. (2007) argue (based on AGN stellar population studies) that there is a 50–100 Myr delay between the peak of nuclear starburst activity and the onset of AGN activity. These studies were however done on AGN selected sources. AGNs plausibly last much longer after the initial feeding event than does starburst activity. Possibly this is because once the central $\sim$1 pc scale accretion disk is fueled with gas via a compact starburst long viscous accretion times (up to 10^9 yr. King & Pringle 2007) allow AGN activity to continue long after starburst activity has faded. Given this timescale difference examples of currently active nuclear starbursts in AGN selected samples might well be expected to be rare. Additionally during the initial composite AGN/starburst phase optical obscuration may be very large making such objects hard to be optically identified as AGN. Since COLA is FIR selected and we have used radio observations as the primary means to detect AGN both of the above biases are avoided allowing the detection of the initial phases of composite AGN/starburst activity.

Both our own observations and those of Condon et al. (1991) show a strong correlation between high FIR luminosity and compact high brightness starbursts. Within the IRAS-BGS sample Condon et al. (1991) found that all starbursts with $L_{\mathrm{FIR}} > 10^{11.8}\,L_{\odot}$ were in fact of this high brightness Eddington-limited type. If the correlation between AGN powered VLBI sources and high brightness shown in Figure 8 also holds for this more luminous sample then one would expect all of these to have AGN activity detectable via VLBI. It can be argued that Arp 220 is a clear counter-example since it has high radio brightness and although detected by VLBI this detection is due to SNe and SNRs rather than an AGN core or lobes. However as noted by Parra et al. (2007) within the western nucleus of Arp 220 there exist several candidate sources for a radio AGN. Recent millimeter continuum and ^{12}CO(2–1) spectral line interferometry results by Downes & Eckart (2007) and Sakamoto et al. (2008) strongly bolster the case that a powerful AGN does in fact exist in the western nucleus of Arp 220.

More generally within snapshot 1.4 GHz VLBI observations conducted by Lonsdale et al. (1993),

about 50% of luminous IRAS-BGS sources were detected on global baselines. These detections had however ambiguous interpretations being explainable by both AGN and radio SNe/SNR models. In general, at other wavebands attempts to definitely detect or reject AGN contributions in these very luminous starbursts have also often proved inconclusive. If as predicted by the Thompson et al. (2005) model for Eddington-limited starbursts the gas supply to the central black hole is relatively constant for compact starburst sources we may obtain the same AGN luminosity regardless of $L_{\rm IR}$. It follows that in more intense higher IR luminosity starbursts it may be harder to detect the AGN component in the midst of all the starburst activity. Paradoxically it may be that within the moderate luminosity COLA sample a strong correlation between intense starburst activity and radio AGNs is easier to detect than in more luminous samples. This is firstly because COLA straddles a luminosity range were there are large numbers of both low brightness and Eddington-limited starbursts. Secondly, $L_{\rm IR}$ is not high enough (except for Arp 220) that there is significant confusion in the radio between AGN and starburst induced structure.

It is clear that both the VLBI snapshot observations of COLA-N presented in this paper and the observations of IRAS-BGS sources carried out by Lonsdale et al. (1993) suffer from lack of uv coverage. New long track VLBI observation which produce good quality images would help distinguish star-formation origins of VLBI flux density (by for instance seeing multiple compact VLBI components indicating star-formation, e.g. Parra et al. 2007) from AGN origins (core-jet morphology sources). Observations of half of the VLBI detected COLA-N sources have already been made using the EVN at 6 cm wavelength. These data are presently being reduced.

6. Conclusions

The main conclusions of this paper are:

1 We have made 4.8 GHz VLA images for 95 of the 110 sources in the COLA North sample. Of these sources 28, 62 and 5 sources have respectively Core, Core+Extended and Extended radio morphologies as defined by Neff & Hutchings (1992). The 15 non-detected sources are likely extended (resolved out) galaxies with radio surface brightnesses below our sensitivity (see §4.2).

2 We argue that the properties of the 4.8 GHz radio emission structures imaged on scales of a few 100 pc are consistent with being powered by star formation activity because the recovered flux density in these structures follows the FIR to radio correlation for star forming galaxies (see §4.1).

3 We detect 22% (20/90) of the sources observed in the VLBI snapshots (see §4.3). Assuming that these VLBI detections are single Gaussian components the simultaneous detection at multiple baselines in most cases constrains the size of the emitting region to parsec scales.

4 The majority of the VLBI detections are well above our detection threshold (see Figure 4) suggesting a lower limit of $\sim 10^{21}\,{\rm W\,Hz^{-1}}$ for the luminosity of these compact sources.

5 Based on luminosity arguments we can rule out a radio supernova remnant (SNR) origin for all of the VLBI detections (see §5.1.3).

6 We can also rule out a radio supernova (SN) origin for most VLBI detections unless we assume that the incidence of powerful radio supernovae is much larger in COLA sources than in most galactic disks. We estimate that at most one or two of the VLBI detections could be due to radio SN.

7 Our VLBI detections are preferentially found in sources with the highest radio brightness arcsecond-scale radio emission, even after subtracting off the VLBI cores. Since this arcsec-scale radio emission is powered by star-formation activity (see point 2 above) we conclude that there is a relationship between compact starbursts and AGN activity. This is consistent with the proposal of Thompson et al. (2005) that Eddington-limited nuclear starbursts can feed AGN.

8 The high AGN incidence amongst compact starbursts implies no significant delay between the period of intense nuclear starburst activity and the

onset of AGN activity. If the AGN activity continues long after the starburst has faded this would explain the predominance of post starburst stellar populations in AGN sources.

We would like to thank the anonymous referee for his/her very helpful comments on an earlier version of this paper. RP acknowledges a Chalmers University PhD student stipend and FONDECYT postdoctoral research grant 3085032. JC acknowledges a Swedish VR grant. The European VLBI Network is a joint facility of European, Chinese, South African and other radio astronomy institutes funded by their national research councils. The Arecibo Observatory is the principal facility of the National Astronomy and Ionosphere Center which is operated by Cornell University under a cooperative agreement with the National Science Foundation. The National Radio Astronomy Observatory is a facility of the National Science Foundation operated under a cooperative agreement by Associated Universities, Inc. This research has made use of the NASA/IPAC Extragalactic Database (NED) which is operated by the Jet Propulsion Laboratory, California Institute of Technology, under contract with the National Aeronautics and Space Administration.

REFERENCES

Arribas, S., Colina, L., & Clements, D. 2001, ApJ, 560, 160

Baldwin, J. A., Phillips, M. M., & Terlevich, R. 1981, PASP, 93, 5

Beichman, C. A., Neugebauer, G., Habing, H. J., Clegg, P. E., & Chester, T. J., eds. 1988, Infrared astronomical satellite (IRAS) catalogs and atlases. Volum e 1: Explanatory supplement

Chandra, P., Stockdale, C. J., Chevalier, R. A., Van Dyk, S. D., Ray, A., Kelley, M. T., Weiler, K. W., Panagia, N., & Sramek, R. A. 2009, ApJ, 690, 1839

Chevalier, R. A. 2006, ArXiv: 0607422

Chomiuk, L. & Wilcots, E. M. 2009, ApJ, 703, 370

Condon, J. J. 1992, ARA&A, 30, 575

Condon, J. J., Cotton, W. D., Greisen, E. W., Yin, Q. F., Perley, R. A., Taylor, G. B., & Broderick, J. J. 1998, AJ, 115, 1693

Condon, J. J., Huang, Z.-P., Yin, Q. F., & Thuan, T. X. 1991, ApJ, 378, 65

Corbett, E. A., Kewley, L., Appleton, P. N., Charmandaris, V., Dopita, M. A., Heisler, C. A., Norris, R. P., Zezas, A., & Marston, A. 2003, ApJ, 583, 670

Corbett, E. A., Norris, R. P., Heisler, C. A., Dopita, M. A., Appleton, P., Struck, C., Murphy, T., Marston, A., Charmandaris, V., Kewley, L., & Zezas, A. L. 2002, ApJ, 564, 650

Davies, R. I., Sánchez, F. M., Genzel, R., Tacconi, L. J., Hicks, E. K. S., Friedrich, S., & Sternberg, A. 2007, ApJ, 671, 1388

Dopita, M. A., Heisler, C., Lumsden, S., & Bailey, J. 1998, ApJ, 498, 570

Downes, D. & Eckart, A. 2007, A&A, 468, L57

Falcke, H. & Biermann, P. L. 1995, A&A, 293, 665

Fathi, K., Storchi-Bergmann, T., Riffel, R. A., Winge, C., Axon, D. J., Robinson, A., Capetti, A., & Marconi, A. 2006, ApJ, 641, L25

Häring, N. & Rix, H.-W. 2004, ApJ, 604, L89

Heckman, T. M. 2008, ArXiv:0809.1101

Helou, G., Soifer, B. T., & Rowan-Robinson, M. 1985, ApJ, 298, L7

Hinshaw, G., Weiland, J. L., Hill, R. S., Odegard, N., Larson, D., Bennett, C. L., Dunkley, J., Gold, B., Greason, M. R., Jarosik, N., Komatsu, E., Nolta, M. R., Page, L., Spergel, D. N., Wollack, E., Halpern, M., Kogut, A., Limon, M., Meyer, S. S., Tucker, G. S., & Wright, E. L. 2009, ApJS, 180, 225

Kauffmann, G., Heckman, T. M., Tremonti, C., Brinchmann, J., Charlot, S., White, S. D. M., Ridgway, S. E., Brinkmann, J., Fukugita, M., Hall, P. B., Ivezić, Ž., Richards, G. T., & Schneider, D. P. 2003, MNRAS, 346, 1055

Kellermann, K. I., Fomalont, E. B., Mainieri, V., Padovani, P., Rosati, P., Shaver, P., Tozzi, P., & Miller, N. 2008, ApJS, 179, 71

Kewley, L. J., Dopita, M. A., Sutherland, R. S., Heisler, C. A., & Trevena, J. 2001, ApJ, 556, 121

Kewley, L. J., Groves, B., Kauffmann, G., & Heckman, T. 2006, MNRAS, 372, 961

Kewley, L. J., Heisler, C. A., Dopita, M. A., Sutherland, R., Norris, R. P., Reynolds, J., & Lumsden, S. 2000, ApJ, 530, 704

King, A. R. & Pringle, J. E. 2007, MNRAS, 377, L25

Knapen, J. 2004, in Astronomical Society of the Pacific Conference Series, Vol. 320, ASP Conf. Ser. 320: The Neutral ISM in Starburst Galaxies, ed. S. Aalto, S. Huttemeister, & A. Pedlar, 205–+

Lonsdale, C. J., Diamond, P. J., Thrall, H., Smith, H. E., & Lonsdale, C. J. 2006, ApJ, 647, 185

Lonsdale, C. J., Smith, H. J., & Lonsdale, C. J. 1993, ApJ, 405, L9

Magorrian, J., Tremaine, S., Richstone, D., Bender, R., Bower, G., Dressler, A., Faber, S. M., Gebhardt, K., Green, R., Grillmair, C., Kormendy, J., & Lauer, T. 1998, AJ, 115, 2285

Merloni, A., Heinz, S., & di Matteo, T. 2003, MNRAS, 345, 1057

Mould, J. R., Huchra, J. P., Freedman, W. L., Kennicutt, Jr., R. C., Ferrarese, L., Ford, H. C., Gibson, B. K., Graham, J. A., Hughes, S. M. G., Illingworth, G. D., Kelson, D. D., Macri, L. M., Madore, B. F., Sakai, S., Sebo, K. M., Silbermann, N. A., & Stetson, P. B. 2000, ApJ, 529, 786

Neff, S. G. & Hutchings, J. B. 1992, AJ, 103, 1746

Norris, R. P., Afonso, J., Appleton, P. N., Boyle, B. J., Ciliegi, P., Croom, S. M., Huynh, M. T., Jackson, C. A., Koekemoer, A. M., Lonsdale, C. J., Middelberg, E., Mobasher, B., Oliver, S. J., Polletta, M., Siana, B. D., Smail, I., & Voronkov, M. A. 2006, AJ, 132, 2409

Parra, R. 2007, PhD thesis, Chalmers Tekniska Hogskola (Sweden)

Parra, R., Conway, J. E., Diamond, P. J., Thrall, H., Lonsdale, C. J., Lonsdale, C. J., & Smith, H. E. 2007, ApJ, 659, 314

Pearson, T. J. 1999, in ASP Conf. Ser. 180: Synthesis Imaging in Radio Astronomy II, ed. G. B. Taylor, C. L. Carilli, & R. A. Perley, 335–+

Prandoni, I., Gregorini, L., Parma, P., de Ruiter, H. R., Vettolani, G., Wieringa, M. H., & Ekers, R. D. 2000, A&AS, 146, 41

Prieto, M. A., Maciejewski, W., & Reunanen, J. 2005, AJ, 130, 1472

—. 2007, AJ, 133, 1847

Rovilos, E., Diamond, P. J., Lonsdale, C. J., Lonsdale, C. J., & Smith, H. E. 2003, MNRAS, 342, 373

Rupen, M. P., van Gorkom, J. H., Knapp, G. R., Gunn, J. E., & Schneider, D. P. 1987, AJ, 94, 61

Rush, B., Malkan, M. A., & Spinoglio, L. 1993, ApJS, 89, 1

Sakamoto, K., Wang, J., Wiedner, M. C., Wang, Z., Peck, A. B., Zhang, Q., Petitpas, G. R., Ho, P. T. P., & Wilner, D. J. 2008, ArXiv e-prints, 806

Sanders, D. B., Mazzarella, J. M., Kim, D.-C., Surace, J. A., & Soifer, B. T. 2003, AJ, 126, 1607

Sanders, D. B. & Mirabel, I. F. 1996, ARA&A, 34, 749

Schartmann, M., Burkert, A., Krause, M., Camenzind, M., Meisenheimer, K., & Davies, R. I. 2010, MNRAS, 219

Smartt, S. J., Eldridge, J. J., Crockett, R. M., & Maund, J. R. 2009, MNRAS, 395, 1409

Smith, H. E., Lonsdale, C. J., & Lonsdale, C. J. 1998, ApJ, 492, 137

Thompson, T. A., Quataert, E., & Murray, N. 2005, ApJ, 630, 167

van Buren, D. & Greenhouse, M. A. 1994, ApJ, 431, 640

van Dyk, S. D., Weiler, K. W., Sramek, R. A., Schlegel, E. M., Filippenko, A. V., Panagia, N., & Leibundgut, B. 1996, AJ, 111, 1271

Veilleux, S. & Osterbrock, D. E. 1987, ApJS, 63, 295

Wunderlich, E., Wielebinski, R., & Klein, U. 1987, A&AS, 69, 487

Yuan, T., Kewley, L. J., & Sanders, D. B. 2010, ApJ, 709, 884

Yun, M. S., Reddy, N. A., & Condon, J. J. 2001, ApJ, 554, 803

Zamfir, S., Sulentic, J. W., & Marziani, P. 2008, MNRAS, 387, 856

This 2-column preprint was prepared with the AAS LaTeX macros v5.2.

TABLE 1 (FULL VERSION)
COLA NORTH SAMPLE

IRAS Name (1)	Other Name (2)	R.A. J2000 (3)	Decl. J2000 (4)	$V_{\rm Hel}$ [km s^{-1}] (5)	D_L [Mpc] (6)	$\log L_{\rm IR}$ [$L_\odot$] (7)	$\log L_{1.4}$ [W Hz^{-1}] (8)	$\log L_{\rm FIR}$ [W Hz^{-1}] (9)	$q_{1.4}$ (10)
00005+2140	MRK334	00 03 09.74	21 57 36.46	6579	93.4	11.07	22.46	24.74	2.27
00073+2538	N23	00 09 53.58	25 55 26.40	4566	64.7	11.09	22.57	24.82	2.25
00506+7248		00 54 04.00	73 05 11.70	4706	69.3	11.49	22.82	25.21	2.40
00521+2858		00 54 50.27	29 14 47.60	4629	65.2	10.88	22.39	24.62	2.23
00548+4331	N317	00 57 40.58	43 47 32.30	5429	77.2	11.16	22.66	24.92	2.26
00555+7614		*00 59 15*	*76 30 52*	4739	70.1	10.91	22.53	24.66	2.13
01503+1227		01 52 59.52	12 42 27.90	4558	63.3	10.91	22.36	24.65	2.29
01519+3640		01 54 53.93	36 55 04.40	5621	79.2	11.02	22.14	24.74	2.60
01555+0250	ARP126	01 58 05.26	03 05 00.90	5431	75.6	10.94	22.47	24.68	2.20
01556+2507		01 58 30.63	25 21 36.90	4916	68.8	10.99	22.36	24.75	2.39
01579+5015		02 01 09.65	50 30 25.50	4875	69.5	10.85	22.29	24.55	2.26
02071+3857	N828	02 10 09.52	39 11 25.30	5374	75.8	11.33	22.85	25.07	2.22
02080+3725	N834	*02 11 01*	*37 39 58*	4593	64.7	10.95	22.49	24.69	2.20
02152+1418	N877	02 17 58.62	14 32 25.90	3913	54.2	10.98	22.58	24.74	2.17
02208+4744		02 24 08.00	47 58 10.68	4679	66.5	11.09	22.51	24.84	2.33
02253+1922	ARP276	*02 28 11*	*19 35 45*	4141	57.5	10.62	22.32	24.37	2.05
02345+2053	N992	02 37 25.43	21 06 09.41	4150	57.6	11.03	22.51	24.76	2.25
02346+3412		02 37 40.04	34 25 54.00	4915	69.0	10.87	22.04	24.59	2.55
02395+3433	N1050	02 42 35.62	34 45 48.97	3901	54.8	10.76	22.06	24.45	2.39
02435+1253		02 46 17.51	13 05 44.56	6560	91.8	11.31	22.86	25.08	2.21
02438+2122		02 46 39.15	21 35 10.37	6987	98.1	11.14	22.31	24.91	2.60
02509+1248	ARP200	02 53 41.50	13 00 48.67	3640	50.4	10.85	22.43	24.59	2.16
02511+1238		02 53 50.30	12 50 56.54	3568	49.4	10.51	21.86	24.26	2.40
02533+0029		02 55 57.25	00 41 33.04	4142	57.4	10.85	22.07	24.61	2.55
02568+3637		02 59 58.61	36 49 13.79	3605	50.8	10.93	22.49	24.62	2.13
02572+7002		03 01 59.72	70 14 30.45	4890	71.5	10.94	22.42	24.67	2.25
03164+4119	3C84	03 19 48.10	41 30 42.00	5264	74.5	11.26	24.27	24.75	0.48
03251+3958		03 28 27.68	40 09 17.04	4262	60.3	10.85	22.27	24.51	2.24
03266+4139	N1334	*03 30 02*	*41 49 55*	4274	60.6	10.78	21.77	24.50	2.73
03406+3908		03 43 56.89	39 17 42.50	4963	70.2	10.88	22.36	24.61	2.25
03449+7252		03 50 36.28	73 01 52.86	4312	63.7	10.85	22.13	24.61	2.48
03514+1546		03 54 15.96	15 55 43.29	6662	93.7	11.18	22.55	24.90	2.35
04002+0149		04 02 48.15	01 57 56.65	3813	53.1	10.67	22.09	24.41	2.32
04007+2201		04 03 44.05	22 09 32.91	6261	88.1	11.08	22.51	24.83	2.32
04097+0525		*04 12 22*	*05 32 51*	5305	74.4	11.19	22.78	24.93	2.15
04356+6738		04 40 47.32	67 44 09.32	4830	70.8	10.93	22.09	24.56	2.47
04435+1822		04 46 29.67	18 27 39.16	4615	63.3	10.78	22.21	24.49	2.28
04520+0311	N1691	04 54 38.38	03 16 04.48	4619	65.2	10.93	22.37	24.68	2.31
05054+1718		05 08 21.21	17 22 08.29	5454	77.4	11.20	22.37	24.97	2.60
05091+0508	N1819	05 11 46.10	05 12 02.22	4470	63.3	10.91	22.31	24.67	2.36
05134+5811		05 17 47.58	58 14 19.18	5320	77.3	10.96	22.54	24.70	2.16
05179+0845		05 20 40.79	08 48 31.20	4687	66.6	11.09	22.61	24.86	2.26
05336+5407		05 37 46.84	54 09 45.79	5392	78.3	10.89	22.19	24.66	2.47
05365+6921	ARP184	05 42 04.65	69 22 42.35	3934	58.6	10.97	22.85	24.72	1.87
05405+0035		05 43 05.51	00 37 12.89	4318	61.8	10.93	22.01	24.70	2.69
05414+5840		05 45 47.97	58 42 04.50	4455	65.3	11.27	22.84	25.06	2.21
06052+8027		*06 14 30*	*80 27 00*	3921	59.3	11.00	22.61	24.76	2.15
06140+8220		06 24 57.70	82 19 06.56	4317	65.0	10.76	22.57	24.48	1.91
06239+7428		06 30 29.73	74 26 31.35	5375	79.7	10.98	22.18	24.71	2.53
06538+4628		06 57 34.42	46 24 10.51	6401	93.7	11.31	22.82	25.05	2.22
07062+2041		07 09 12.38	20 36 14.56	5227	76.7	11.09	22.66	24.83	2.17
07063+2043	N2342	07 09 18.08	20 38 09.67	5276	77.4	11.30	22.82	25.03	2.20
07204+3332		07 23 43.52	33 26 31.38	4031	60.1	10.88	22.19	24.59	2.40
F07258+3357	N2388	*07 28 53*	*33 49 09*	4134	61.7	11.24	22.53	25.00	2.47
07258+3357	N2389	07 29 04.64	33 51 39.10	3957	59.1	10.75	22.18	24.52	2.34
07329+1149		07 35 43.42	11 42 35.31	4873	72.3	11.10	22.46	24.87	2.41
07336+3521	N2415	*07 36 57*	*35 14 31*	3784	56.9	10.92	22.41	24.66	2.25

TABLE 1 (FULL VERSION)—*Continued*

IRAS Name (1)	Other Name (2)	R.A. J2000 (3)	Decl. J2000 (4)	$V_{\rm Hel}$ [km s^{-1}] (5)	D_L [Mpc] (6)	$\log L_{\rm IR}$ [$L_\odot$] (7)	$\log L_{1.4}$ [W Hz^{-1}] (8)	$\log L_{\rm FIR}$ [W Hz^{-1}] (9)	$q_{1.4}$ (10)
07566+2507	N2498	07 59 38.79	24 58 56.73	4720	70.7	10.86	22.03	24.60	2.57
08287+5246		08 32 28.07	52 36 21.14	5094	76.6	10.94	22.06	24.67	2.61
08339+6517		08 38 23.42	65 07 14.12	5730	85.7	11.11	22.47	24.81	2.34
08354+2555	ARP243	08 38 24.08	25 45 16.57	5549	83.6	11.59	22.90	25.39	2.49
08561+0629	N2718	08 58 50.47	06 17 34.88	3843	59.4	10.66	22.10	24.37	2.27
09437+0317	I563	*09 46 22*	*03 03 16*	6136	94.3	11.26	22.56	24.97	2.41
10195+2149	N3221	*10 22 20*	*21 34 10*	4110	65.2	11.05	22.77	24.80	2.04
11413+1103	N3839	11 43 54.02	10 47 08.24	5916	93.6	11.04	22.70	24.80	2.10
11547+2528	N3987	11 57 20.92	25 11 42.60	4502	72.6	10.98	22.55	24.76	2.21
12099+2926	N4175	12 12 31.03	29 10 06.28	4012	65.5	10.87	22.36	24.63	2.27
12159+3005	N4253	12 18 26.52	29 48 46.51	3876	63.5	10.79	22.26	24.39	2.12
12208+0744	N4334	12 23 23.87	07 28 23.35	4245	69.3	10.88	22.18	24.61	2.43
13126+2452	IC860	13 15 03.51	24 37 07.78	3347	56.4	11.11	22.07	24.92	2.85
13183+3423	ARP193	13 20 35.33	34 08 22.24	6985	109.0	11.70	23.17	25.49	2.32
13188+0036	N5104	13 21 23.13	00 20 32.90	5578	90.2	11.22	22.57	24.99	2.42
13238+3611	N5149	13 26 09.13	35 56 02.77	5652	89.7	11.06	22.41	24.81	2.40
13373+0105	ARP240	*13 39 55*	*00 50 02*	6745	107.0	11.61	22.76	25.33	2.57
13470+3530		13 49 15.53	35 15 46.77	5032	80.9	11.14	22.87	24.90	2.03
14003+3245	N5433	14 02 36.04	32 30 36.40	4354	71.2	10.99	22.58	24.74	2.16
14221+2450	N5610	14 24 22.92	24 36 51.15	5063	82.0	11.02	22.40	24.75	2.35
14280+3126	N5653	*14 30 10*	*31 12 57*	3562	59.7	11.12	22.49	24.85	2.36
15005+8343		14 56 06.77	83 31 22.08	3881	60.0	10.78	22.10	24.48	2.38
15107+0724		15 13 13.10	07 13 31.85	3897	65.0	11.32	22.43	25.15	2.72
15276+1309	N5936	15 30 00.84	12 59 21.45	4004	66.6	11.10	22.88	24.83	1.95
15327+2340	ARP220	15 34 57.25	23 30 11.41	5434	87.3	12.27	23.47	26.07	2.60
15437+0234	N5990	15 46 16.37	02 24 55.69	3839	63.9	11.11	22.51	24.81	2.31
16030+2040	ARP209	16 05 12.79	20 34 38.38	4739	77.1	11.06	22.87	24.79	1.92
16478+6303	N6247	16 48 19.01	62 58 41.33	4480	70.2	10.85	22.37	24.59	2.21
16577+5900	ARP293	16 58 31.74	58 56 14.65	5501	85.1	11.31	23.13	25.10	1.96
17180+6039	N6361	*17 18 41*	*60 36 29*	3881	60.6	10.81	22.30	24.56	2.26
17468+1320		17 49 06.20	13 19 55.57	4881	77.9	11.01	22.38	24.82	2.44
17530+3446		*17 54 52*	*34 46 34*	4881	77.0	11.09	22.57	24.82	2.25
17548+2401		17 56 56.64	24 01 01.88	5944	92.8	11.18	22.74	24.96	2.22
18131+6820	ARP81	18 12 55.37	68 21 48.24	6191	93.6	11.26	22.41	25.00	2.59
18145+2205		18 16 40.68	22 06 46.20	5599	87.5	11.16	22.46	24.93	2.47
18263+2242		18 28 23.92	22 44 11.60	4071	65.1	10.77	22.03	24.51	2.48
18425+6036		18 43 10.62	60 39 29.55	3965	61.9	11.10	22.61	24.86	2.25
18495+2334		18 51 37.75	23 38 05.39	4559	71.6	10.81	22.12	24.53	2.41
19000+4040	N6745	19 01 41.24	40 45 04.69	4545	70.7	11.01	22.71	24.75	2.05
22025+4205		22 04 36.00	42 19 39.46	4290	63.5	11.02	22.23	24.80	2.58
22171+2908	ARP27	22 19 27.73	29 23 44.87	4569	66.9	10.94	22.59	24.70	2.11
22388+3359		22 41 12.24	34 14 56.51	6413	92.8	11.33	22.60	25.09	2.49
23007+0836	ARP298	23 03 15.62	08 52 26.06	4892	70.3	11.63	23.02	25.32	2.30
23106+0603		23 13 12.75	06 19 18.11	3536	51.0	10.69	21.52	24.29	2.76
23157+0618		23 18 16.28	06 35 09.03	4966	70.9	11.05	22.50	24.80	2.31
23213+0923		23 23 54.07	09 40 02.10	3559	51.1	10.58	21.72	24.33	2.60
23262+0314	ARP216	23 28 46.67	03 30 41.00	5138	73.3	11.13	22.55	24.83	2.28
23414+0014	N7738	23 44 02.04	00 30 59.84	6762	96.3	11.11	22.57	24.86	2.29
23445+2911	ARP86	*23 47 02*	*29 28 23*	4845	69.1	10.95	22.32	24.71	2.39
23485+1952	N7769	23 51 03.98	20 09 01.52	4211	59.9	10.99	22.41	24.77	2.36
23488+1949	N7771	23 51 24.85	20 06 42.30	4256	58.7	11.31	22.77	25.08	2.32
23488+2018	MRK331	23 51 26.74	20 35 10.33	5541	78.7	11.49	22.72	25.24	2.52
23591+2312	Taffy	00 01 41.91	23 29 45.00	4353	61.8	10.91	22.79	24.66	1.88

COLUMNS— (1): IRAS name (from Point Source Calalog, excepting F07258+3357 which is taken from the Faint Source Catlog). (2): Other name. (3)-(4): Right Ascencion and Declination (from VLA observations, unless undetected in which case IRAS positions are given in italics). VLA positions are conservatively estimated to be accurate to $0.3''$ and IRAS positions to $20''$. (5): Heliocentric velocity (cz) from NED. (6): Luminosity distance (see Section 2). (7): FIR luminosity (see Section 3.3). (8): 1.4 GHz luminosity calculated from the NVSS catalog (Condon et al. 1998). (9): FIR spectral luminosity (see Section 3,3). (10)): $q_\nu = \log(L_{\rm FIR}/L_{1.4})$.

TABLE 3 (FULL VERSION)

RADIO AND OPTICAL OBSERVATIONS AND RESULTS

IRAS Name (1)	VLA Array (2)	VLA Morph (3)	$S_{4.8\ \mathrm{total}}$ (mJy) (4)	$q_{4.8}$ (5)	$S_{4.8\ \mathrm{comp}}$ (mJy) (6)	$\theta_M \times \theta_m$ [$'' \times ''$] (7)	$\log T_b$ [K] (8)	VLBI Epoch (9)	Optical Class (10)
00005+2140	BnA–A	CE	5.66	2.97	0.00	–	–	1*	S
00073+2538	BnA–A	C	18.40	2.85	1.23	0.45×0.22	2.63	1	C
00506+7248	A	CE	31.60	2.95	13.60	1.27×0.66	2.75	2	–
00521+2858	BnA	E	6.07	3.13	3.40	3.15×0.91	1.61	1	–
00548+4331	A	CE	13.21	2.95	13.11	1.51×0.41	2.87	2	–
00555+7614	A	U	–	–	–	–	–	2	–
01503+1227	BnA	CE	6.23	3.18	5.25	1.58×1.03	2.05	1	C
01519+3640	A	CE	4.38	3.23	3.92	1.13×0.74	2.21	1-2	C
01555+0250	BnA	CE	8.23	2.92	1.85	2.04×1.06	1.47	–	L
01556+2507	BnA	CE	11.16	2.95	7.37	1.32×1.02	2.28	1	H
01579+5015	A	CE	2.49	3.39	1.82	0.59×0.38	2.45	2	L
02071+3857	A	E	12.20	3.15	0.93	0.85×0.56	1.83	2	–
02080+3725	A	U	–	–	–	–	–	1-2	H
02152+1418	BnA	CE	2.39	3.82	1.34	1.49×0.94	1.52	1-2	–
02208+4744	A	CE	10.92	3.08	10.61	1.78×1.02	2.31	2	–
02253+1922	BnA	U	–	–	–	–	–	1-2	H
02345+2053	BnA	CE	14.69	2.99	3.61	1.90×1.20	1.74	1-2	C
02346+3412	A	CE	4.88	3.15	4.06	2.16×1.28	1.71	1-2	H
02395+3433	A	C	3.62	3.34	2.98	0.53×0.40	2.69	2	C
02435+1253	BnA	CE	20.60	2.76	14.98	4.21×1.44	1.93	1-2	S
02438+2122	BnA	C	17.44	2.61	17.40	0.28×0.10	4.33	2	L
02509+1248	BnA	CE	11.38	3.05	3.16	2.11×1.32	1.59	–	C
02511+1238	BnA	CE	5.34	3.07	3.26	1.91×1.51	1.59	1-2	H
02533+0029	BnA-A	CE	4.65	3.35	7.06	0.60×0.54	2.88	–	H
02568+3637	A	CE	28.16	2.68	30.65	2.10×0.69	2.86	2*	S
02572+7002	A	CE	3.78	3.30	1.82	0.81×0.62	2.10	2	–
03164+4119	A	C	49400.00	-0.76	0.00	–	–	1-2*	L
03251+3958	A	CE	4.79	3.19	1.02	1.07×0.24	2.14	2	H
03266+4139	A	U	–	–	–	–	–	–	–
03406+3908	A	C	0.40	4.24	0.41	0.26×0.00	3.04	2	S
03449+7252	A	CE	4.98	3.22	2.12	0.81×0.67	2.13	2	–
03514+1546	BnA	CE	4.07	3.27	3.51	1.56×0.93	1.92	1	–
04002+0149	BnA	CE	5.99	3.10	7.80	4.68×1.78	1.51	–	L
04007+2201	BnA	CE	2.98	3.39	1.31	1.02×0.80	1.74	1	C
04097+0525	A	U	–	–	–	–	–	–	H
04356+6738	A	CE	6.07	3.00	5.61	1.53×1.25	2.01	2	–
04435+1822	BnA–A	C	7.90	2.91	4.64	1.88×0.05	3.23	1-2*	H
04520+0311	BnA	CE	11.04	2.93	4.42	3.42×1.25	1.55	–	C
05054+1718	BnA-A	C	9.45	3.14	7.43	0.33×0.25	3.49	1*	S
05091+0508	BnA	CER	13.06	2.87	0.43	1.15×0.67	1.29	–	C
05134+5811	A	CE	1.62	3.64	0.57	0.27×0.06	3.09	2	–
05179+0845	BnA	CE	3.68	3.57	1.30	1.68×0.97	1.44	–	H
05336+5407	A	CE	5.48	3.06	3.56	0.91×0.34	2.60	2	–
05365+6921	A	C	1.36	3.97	1.45	0.06×0.00	4.22	2	–
05405+0035	BnA	CE	4.99	3.34	5.53	1.42×0.87	2.19	–	H
05414+5840	A	CE	21.80	3.01	15.75	0.83×0.39	3.23	2	–
06052+8027	A	U	–	–	–	–	–	2	–
06140+8220	A	C	57.69	2.02	58.72	0.20×0.04	5.41	2*	–
06239+7428	A	C	1.69	3.60	0.00	–	–	2*	–
06538+4628	A	CE	6.11	3.24	3.97	0.57×0.40	2.78	2	–
07062+2041	BnA	CE	6.77	3.15	2.48	0.97×0.81	2.04	1	H
07063+2043	BnA-A	CE	7.07	3.32	4.55	1.18×0.72	2.27	1	–
07204+3332	A	CE	7.77	3.06	1.68	0.56×0.42	2.39	1-2	–
F07258+3357	A	CE	12.95	3.23	13.26	0.56×0.35	3.37	1-2*	H
07258+3357	A	U	–	–	–	–	–	1	–
07329+1149	BnA	C	10.62	3.05	10.23	0.75×0.55	2.93	1	H

TABLE 3 (FULL VERSION)—*Continued*

IRAS Name (1)	VLA Array (2)	VLA Morph (3)	$S_{4.8\ \mathrm{total}}$ (mJy) (4)	$q_{4.8}$ (5)	$S_{4.8\ \mathrm{comp}}$ (mJy) (6)	$\theta_M \times \theta_m$ [$'' \times ''$] (7)	$\log T_b$ [K] (8)	VLBI Epoch (9)	Optical Class (10)
07336+3521	A	U	–	–	–	–	–	1	–
07566+2507	BnA	CE	3.57	3.27	3.25	1.65×1.07	1.80	1	C
08287+5246	A	CE	4.58	3.17	1.21	0.91×0.45	2.01	2	–
08339+6517	A	CE	6.04	3.08	1.69	0.62×0.48	2.29	2	H
08354+2555	BnA–A	C	71.49	2.61	72.08	0.44×0.30	4.28	1*	-
08561+0629	BnA	CE	2.26	3.39	1.93	2.01×1.32	1.40	–	H
09437+0317	BnA	U	–	–	–	–	–	–	–
10195+2149	BnA	U	–	–	–	–	–	1	–
11413+1103	BnA	CE	8.02	2.88	1.13	2.58×0.78	1.29	1	H
11547+2528	BnA	E	8.68	3.03	9.68	4.81×0.78	1.95	1	–
12099+2926	BnA	E	11.89	2.84	13.26	4.43×1.53	1.83	1	–
12159+3005	BnA	C	14.16	2.55	14.24	0.36×0.26	3.72	1	S
12208+0744	BnA	CE	10.08	2.85	2.37	1.37×0.56	2.03	2	H
13126+2452	A	C	19.96	3.03	20.23	0.20×0.14	4.40	1*	–
13183+3423	A	CE	49.12	2.65	39.13	0.58×0.29	3.91	1-2*	C
13188+0036	BnA	C	7.64	3.11	7.13	1.15×0.78	2.44	2	C
13238+3611	A	CE	6.36	3.02	1.84	0.75×0.52	2.21	1-2	–
13373+0105	BnA	U	–	–	–	–	–	–	–
13470+3530	A	C	3.87	3.42	3.82	0.27×0.07	3.84	1-2*	–
14003+3245	A	CE	9.48	2.98	2.37	0.77×0.51	2.32	1-2	C
14221+2450	A	C	8.40	2.92	5.37	0.35×0.29	3.26	–	C
14280+3126	A	U	–	–	–	–	–	1-2	H
15005+8343	A	CE	5.28	3.13	1.30	1.04×0.49	1.95	2	–
15107+0724	BnA	C	31.69	2.94	32.34	0.30×0.26	4.16	–	C
15276+1309	BnA–A	CE	11.23	3.06	3.40	0.64×0.51	2.56	1	C
15327+2340	BnA	CE	183.13	2.85	97.51	0.21×0.14	5.06	1*	L
15437+0234	BnA	CE	6.69	3.30	6.51	1.99×1.67	1.83	–	S
16030+2040	BnA	CE	14.59	2.78	1.23	0.61×0.31	2.35	1	H
16478+6303	A	E	41.48	2.20	36.32	2.48×1.43	2.55	2*	–
16577+5900	A	C	15.24	2.98	7.80	0.25×0.21	3.71	2*	C
17180+6039	A	U	–	–	–	–	–	2	–
17468+1320	BnA–A	C	24.43	2.57	16.07	0.17×0.13	4.40	1-2*	–
17530+3446	A	U	–	–	–	–	–	1-2	–
17548+2401	BnA–A	C	16.19	2.73	12.08	0.70×0.33	3.26	1*	L
18131+6820	A	CE	6.37	3.18	6.34	2.19×0.59	2.23	2	C
18145+2205	BnA	CE	6.80	3.13	6.30	2.67×0.60	2.13	1	–
18263+2242	BnA–A	CE	3.73	3.23	1.15	0.87×0.52	1.94	1	C
18425+6036	A	CE	15.37	3.01	2.29	0.13×0.00	4.09	2	C
18495+2334	BnA	CE	6.43	2.93	6.95	1.76×1.61	1.93	1	C
19000+4040	A	CE	2.77	3.53	1.38	1.25×0.44	1.94	–	H
22025+4205	A	C	15.72	2.92	13.01	0.48×0.28	3.53	2	–
22171+2908	BnA	C	6.40	3.17	4.28	1.33×0.55	2.31	1	–
22388+3359	A	CE	10.86	3.04	7.03	0.51×0.42	3.06	1-2	C
23007+0836	BnA–A	C	63.66	2.75	46.20	0.33×0.25	4.29	2*	S
23106+0603	BnA–A	CE	6.15	3.00	3.79	0.45×0.22	3.12	–	H-
23157+0618	BnA–A	C	12.04	2.94	12.05	1.02×0.52	2.90	2	S
23213+0923	BnA	CE	5.34	3.10	2.27	1.73×1.36	1.52	–	H
23262+0314	BnA	CE	7.99	3.12	1.52	1.38×0.58	1.82	–	S
23414+0014	BnA–A	CE	10.86	2.78	3.77	0.51×0.23	3.05	2	–
23445+2911	BnA	U	–	–	–	–	–	1	–
23485+1952	BnA	C	0.54	4.40	0.51	0.86×0.40	1.71	1	C
23488+1949	BnA	CER	23.88	3.09	3.30	1.67×1.00	1.84	1*	L
23488+2018	BnA-A	C	31.23	2.87	20.77	1.17×0.73	2.93	1-2*	C
23591+2312	BnA	C	14.09	2.85	2.30	1.63×0.57	1.93	1	C

COLUMNS— (1): IRAS Name (2): VLA array(s) used (3): Morphology class of VLA 4.8GHz image. C-Compact, E-Extended, CE-Compact plus Extended, CER-Compact plus extended with ring, U-Undetected. (4): Recovered 4.8GHz flux density in VLA image. (5). Log of ratio of 4.8GHz recovered VLA flux density to FIR flux density. (6): Total flux density of gaussian fitted to brightest feature in VLA image (after removing VLBI component, hence zero indicates that brightest feature was dominated by the VLBI component). (7): Fitted gaussian major and minor axes to peak VLA feature (FWHM arcsec), Note for IRAS15327+2340 (Arp 220) these are for the western nucleus as taken from the literature (see Section 4.5). (7): Fitted gaussian major and minor axes to peak VLA feature (FWHM arcsec). (8): Peak 4.8GHz brightness temperature of gaussian component (see Section 4.5). Note if formally unresolved along one axis a 50mas FWHM was assumed along that axis). (9): VLBI Epoch(s) observed (asterisk indicates VLBI detection, see Table 4 for details). (10): Optical Class (see Section 4.6) with H=HII, S=Seyfert, L=LINER and C=Composite.

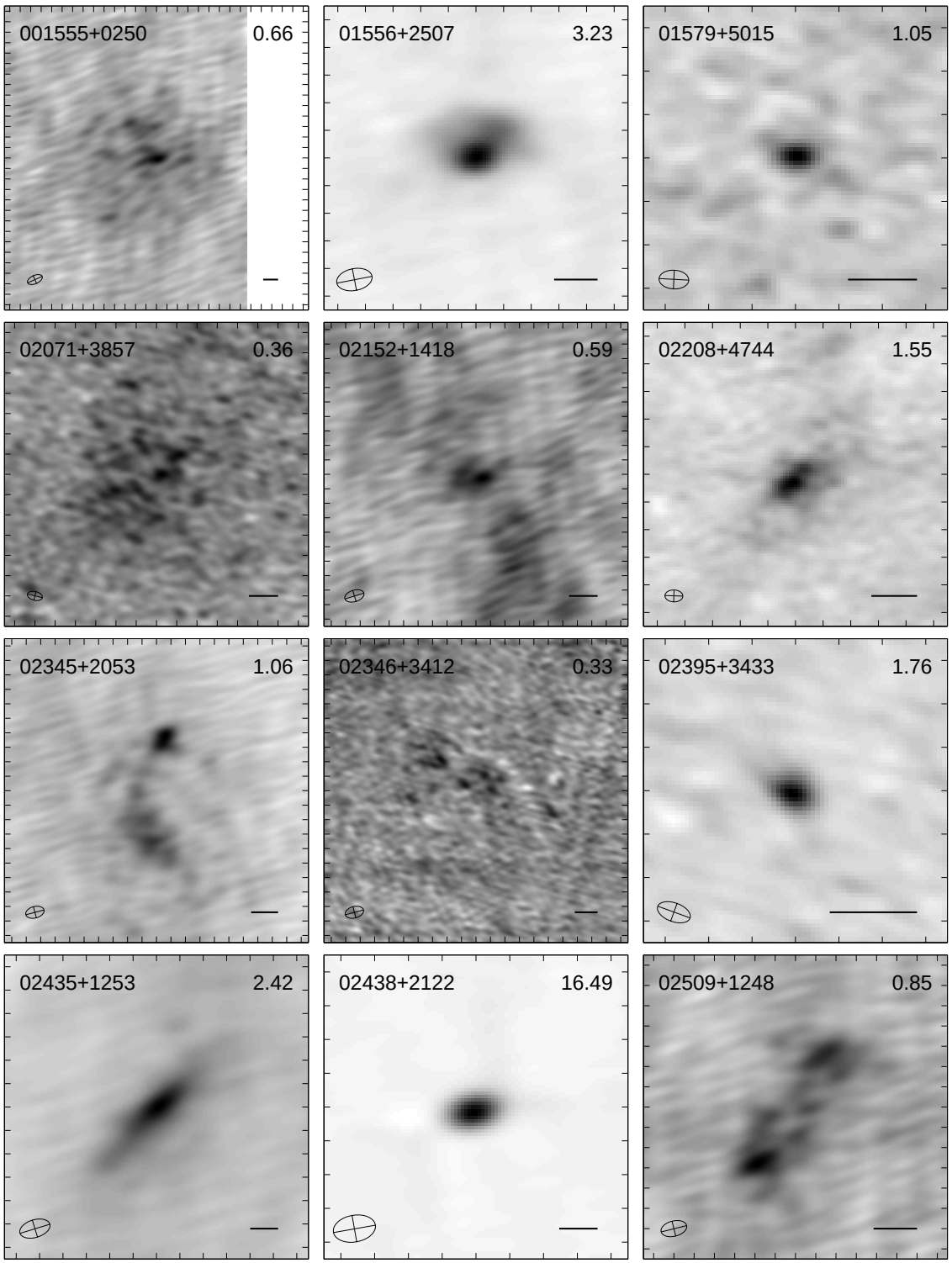

Fig. 3.2.— See caption of Figure 3.1–3.7

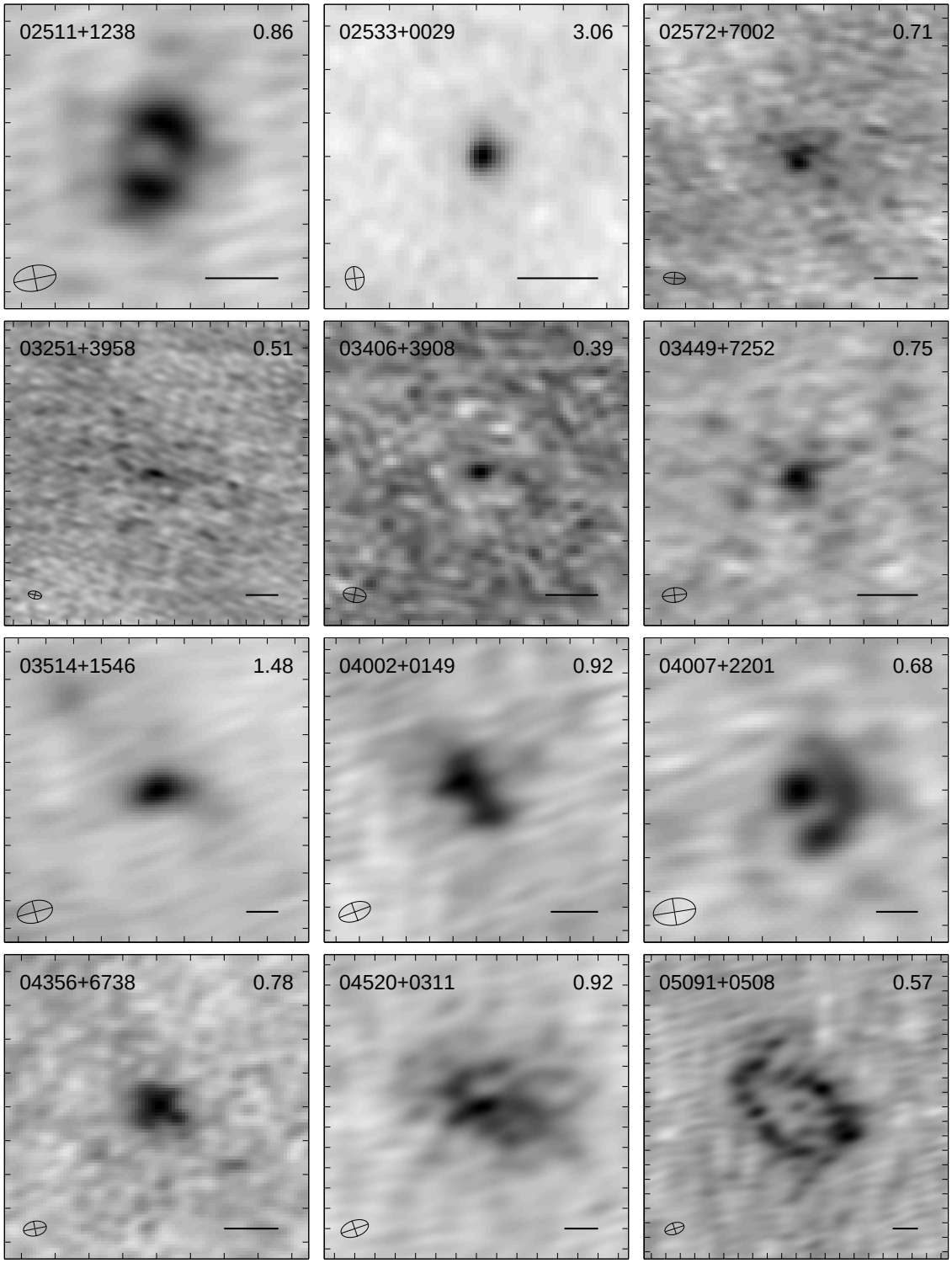

Fig. 3.3.— See caption of Figure 3.1–3.7

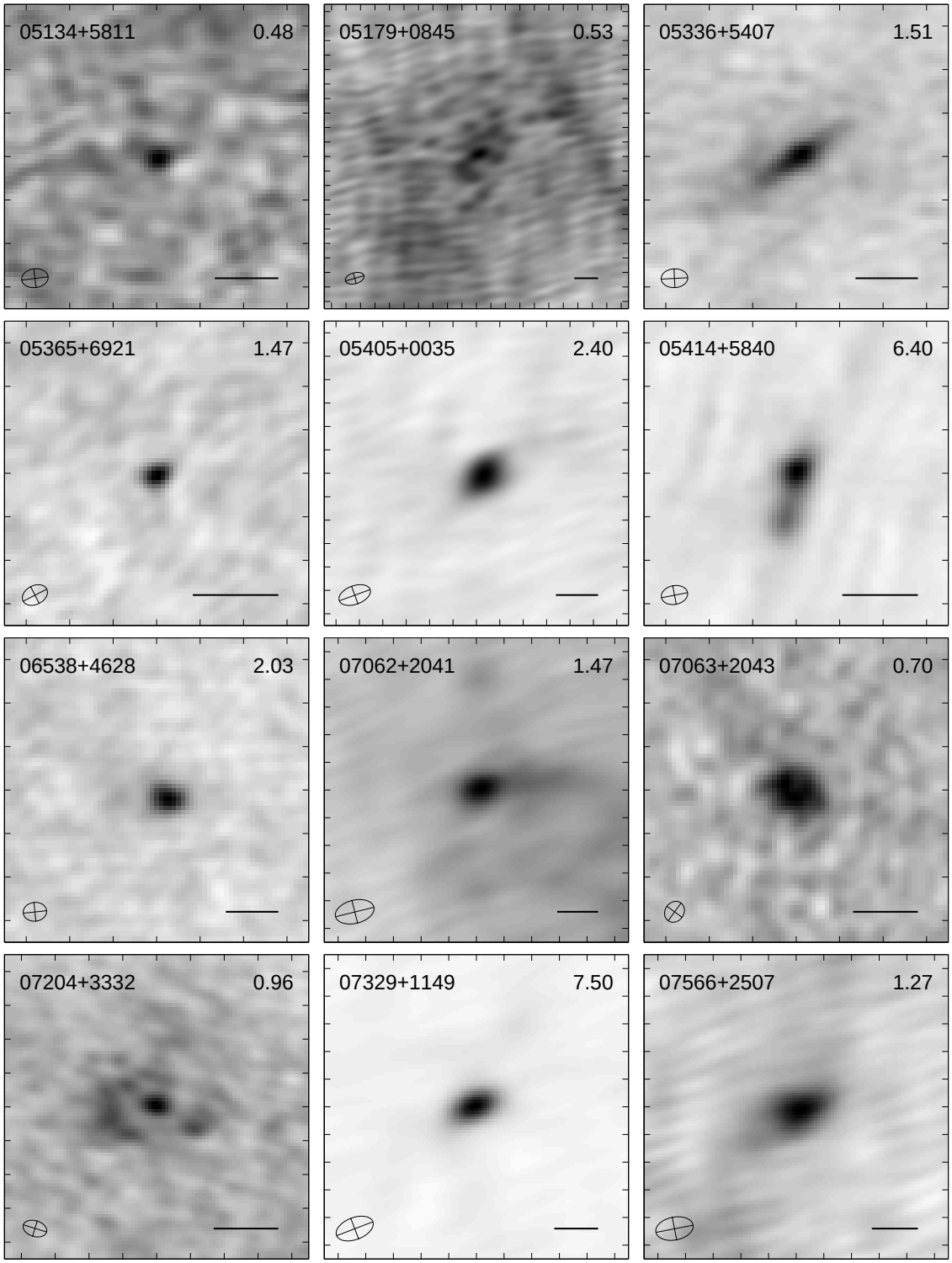

Fig. 3.4.— See caption of Figure 3.1–3.7

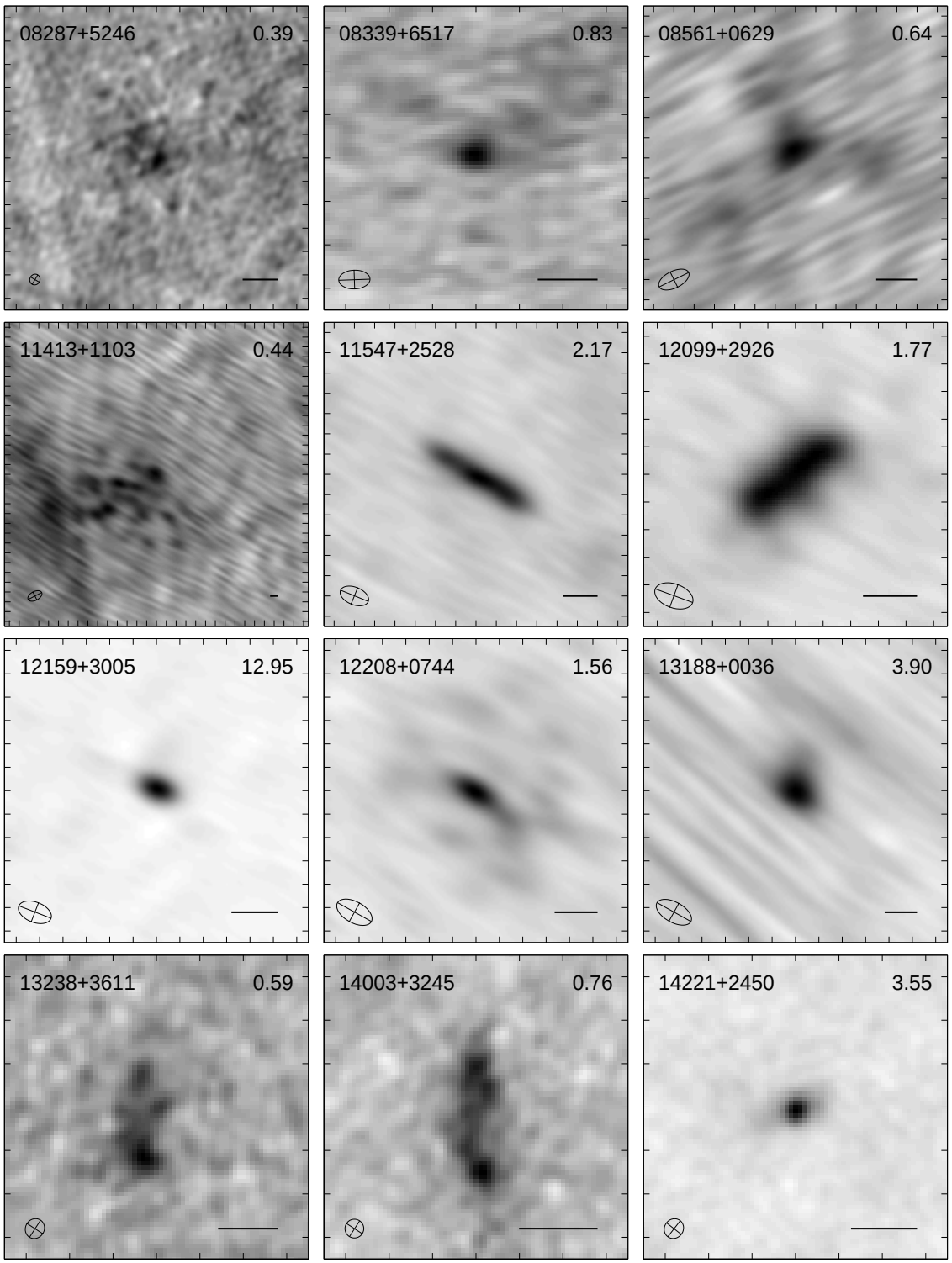

Fig. 3.5.— See caption of Figure 3.1–3.7

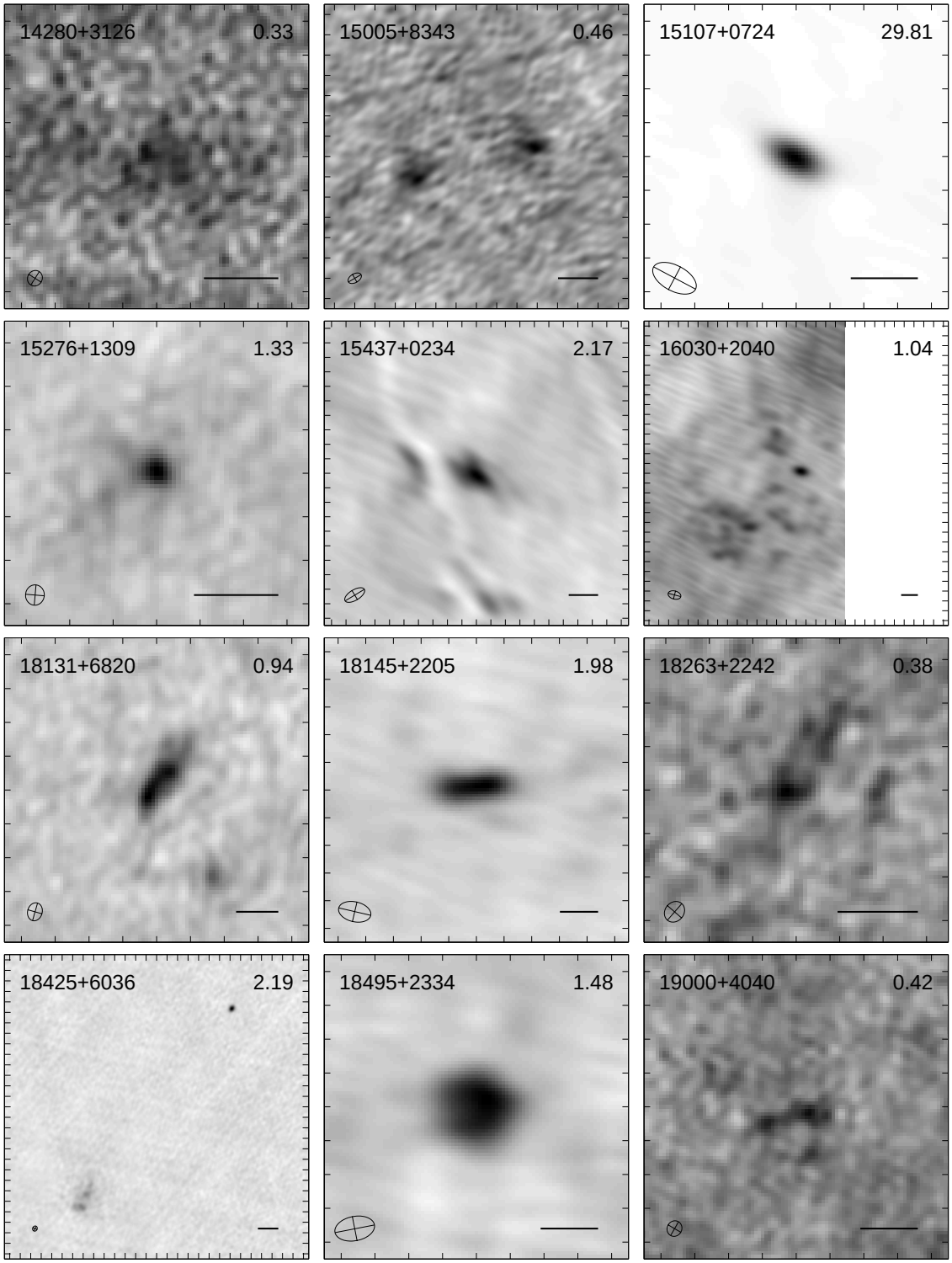

Fig. 3.6.— See caption of Figure 3.1–3.7

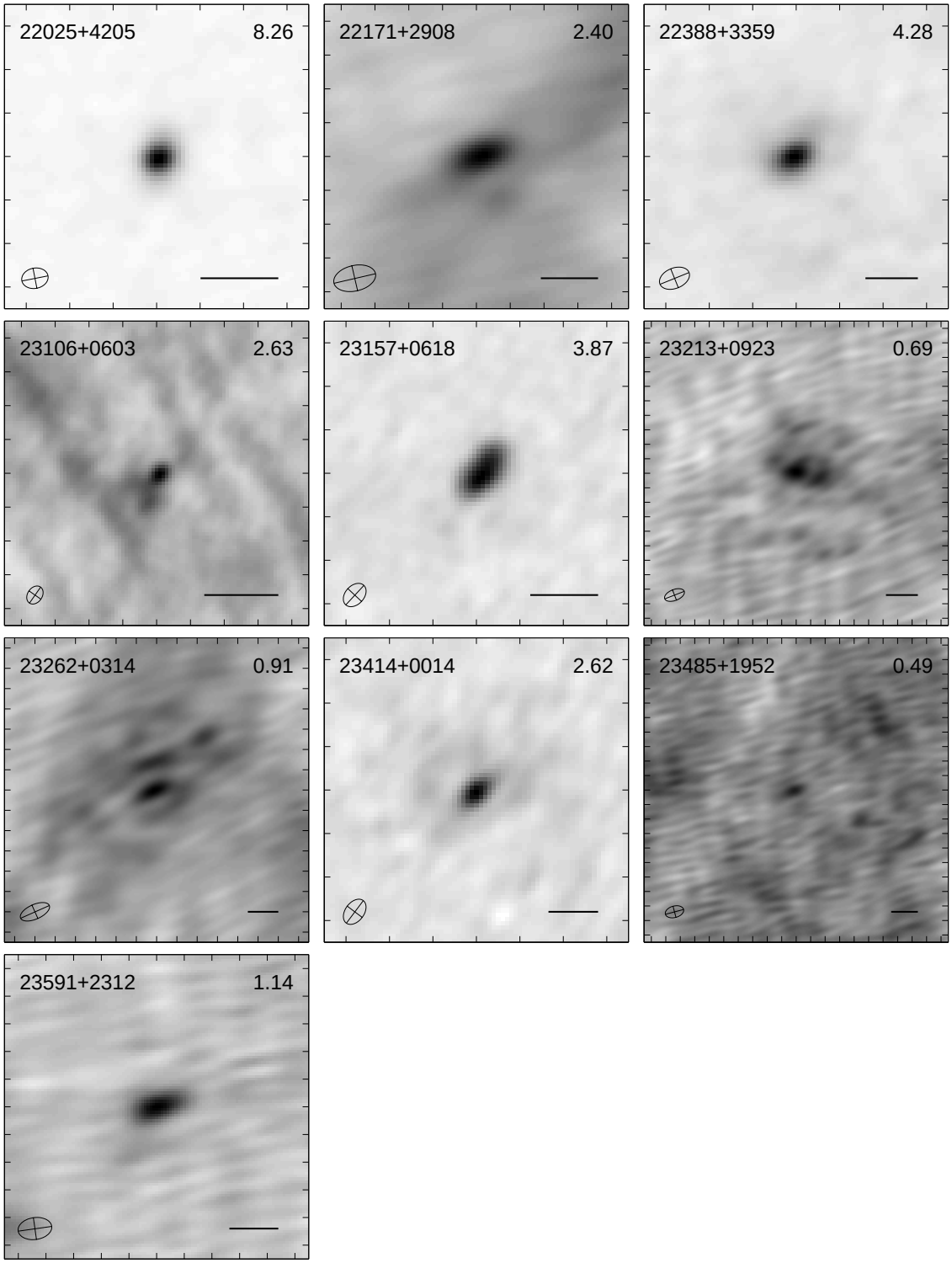

Fig. 3.7.— See caption of Figure 3.1–3.7

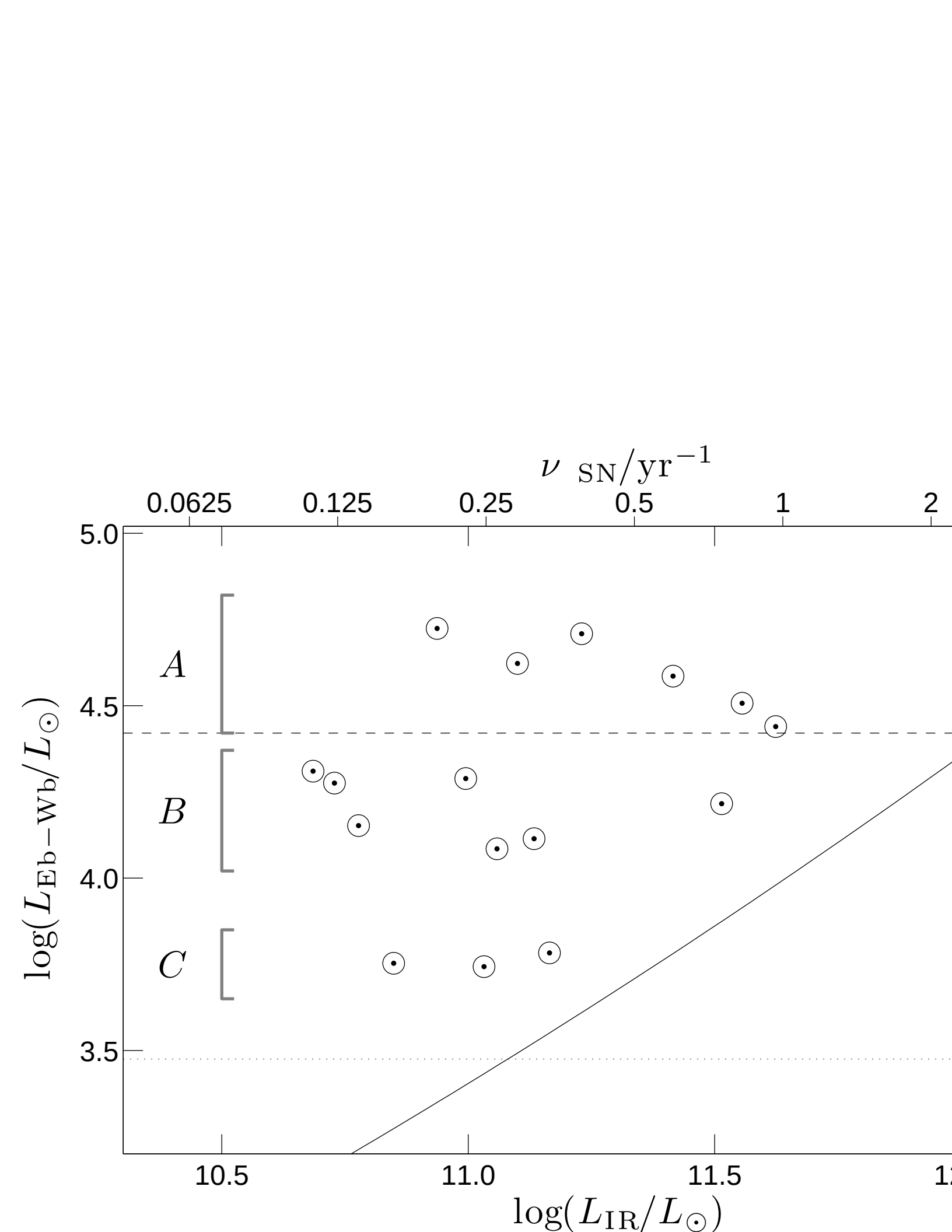
ν SN/yr^{-1}
0.0625
0.125
0.25
0.5
1
2
5.0
4.5
4.0
3.5
A
B
C
$\log(L_{\rm Eb-Wb}/L_\odot)$
10.5
11.0
11.5
$\log(L_{\rm IR}/L_\odot)$